Landon D. Owen[1]
Combustion Research Facility,
Sandia National Laboratories,
Livermore, CA 94550
e-mail: Lndnwn9@gmail.com

Wenjun Ge
Computational Science and Engineering Division,
Oak Ridge National Laboratory,
Oak Ridge, TN 37830

Martin Rieth
Combustion Research Facility,
Sandia National Laboratories,
Livermore, CA 94550

Marco Arienti
Combustion Research Facility,
Sandia National Laboratories,
Livermore, CA 94550

Lucas Esclapez
Computational Science Center,
National Renewable Energy Laboratory,
Golden, CO 80401

Bruno S. Soriano
Combustion Research Facility,
Sandia National Laboratories,
Livermore, CA 94550

Michael E. Mueller
Department of Mechanical and Aerospace
Engineering,
Princeton University,
Princeton, NJ 08544

Marcus Day
Computational Science Center,
National Renewable Energy Laboratory,
Golden, CO 80401

Ramanan Sankaran
Computational Science and Engineering Division,
Oak Ridge National Laboratory,
Oak Ridge, TN 37830

Jacqueline H. Chen
Combustion Research Facility,
Sandia National Laboratories,
Livermore, CA 94550

PeleMP: The Multiphysics Solver for the Combustion Pele Adaptive Mesh Refinement Code Suite

Combustion encompasses multiscale, multiphase reacting flow physics spanning a wide range of scales from the molecular scales, where chemical reactions occur, to the device scales, where the turbulent flow is affected by the geometry of the combustor. This scale disparity and the limited measurement capabilities from experiments make modeling combustion a significant challenge. Recent advancements in high-performance computing (HPC), particularly with the Department of Energy's Exascale Computing Project (ECP), have enabled high-fidelity simulations of practical applications to be performed. The major physics submodels, including chemical reactions, turbulence, sprays, soot, and thermal radiation, exhibit distinctive computational characteristics that need to be examined separately to ensure efficient utilization of computational resources. This paper presents the multiphysics solver for the Pele code suite, called PeleMP, which consists of models for spray, soot, and thermal radiation. The mathematical and algorithmic aspects of the model implementations are described in detail as well as the verification process. The computational performance of these models is benchmarked on multiple supercomputers, including Frontier, an exascale machine. Results are presented from production simulations of a turbulent sooting ethylene flame and a bluff-body swirl stabilized spray flame with sustainable aviation fuels to demonstrate the capability of the Pele codes for modeling practical combustion problems with multiphysics. This work is an important step toward the exascale computing era for high-fidelity combustion simulations providing physical insights and data for predictive modeling of real-world devices. [DOI: 10.1115/1.4064494]

1 Introduction

Driven by the urgency to mitigate climate change while providing clean energy for transportation, power generation, and propulsion, high-fidelity combustion simulations of "real-world" devices that couple myriad scales and multiphysics are required to develop predictive subprocess physics models for engineering

computational fluid dynamics (CFD) simulations. Engineering CFD simulations are needed to shorten the design cycle and cost for next-generation combustors that utilize carbon-neutral alternative fuels. The myriad scales are nonlinearly coupled through reactions at the molecular scale with multiphase mixing through the turbulence cascade, whose largest scales are affected by the geometry of the device. Detailed combustion simulations that are capable of differentiating physical and chemical fuel properties (e.g., hydrogen) or *carbon-neutral* (e.g., sustainable aviation fuels (SAF)) alternative fuels, coupled with turbulent mixing and other multiphysics are needed. Simulations further need to account for differences in soot particle sizes exiting aero-engine combustors for SAFs, which provide ice crystal nucleation sites for downstream contrail formation, a key contributor to global warming from aviation.

Some of the largest previous turbulent combustion simulations have used the S3D code [1]. For example, temporally evolving jet configurations were performed with up to 11 billion cells [2]. However, these simulations represent an idealized combustion configuration do not involve practical geometries, and do not utilize adaptive mesh refinement (AMR).

Recent deployment of exascale heterogeneous supercomputers at the Department of Energy's Leadership Class Computing Facilities at Oak Ridge and Argonne National Laboratories (OLCF and ALCF), Frontier and Aurora, respectively, together with exascale-ready software enabled by the Exascale Computing Project (ECP) has resulted in the *Combustion-Pele* code suite; a direct numerical simulation (DNS) and large eddy simulation (LES) suite of simulation codes and transport and thermochemistry libraries [3–5]. The Pele suite leverages AMR, Lagrangian particle treatment, complex geometry, and math solvers developed as part of ECP through the AMReX and SUNDIALS libraries [6,7]. Ultimately, the Pele code suite can perform simulations involving realistic geometries and multiphysics with tens of billions of cells.

The objective of the present study is to describe a new multiphysics library, referred to as PeleMP, that couples with the Pele compressible and low-Mach codes, PeleC and PeleLMeX respectively. PeleMP includes computationally efficient and scalable models for multicomponent reacting fuel sprays, soot, and thermal radiation that are performant on exascale supercomputers. Sprays are modeled using an Eulerian–Lagrangian treatment for dilute sprays where point particles represent parcels of fuel droplets dispersed in the gas phase and coupled with the reactive flow simulation [8,9]. Soot formation, growth, and oxidation is modeled using the hybrid method of moments (HMOM) developed by Mueller et al. [10]. Thermal radiation is modeled by the spherical harmonics P1 approximation with the Planck-mean spectral model [11], incorporating the radiating gases such as CO_2, H_2O, CO, CH_4, C_2H_4, as well as soot. The aforementioned models are based on the native AMReX and Pele frameworks and data structures so that they can readily be extended to even higher-order models. The Pele suite of codes and libraries is publicly available at the software's GitHub repository[1].

The remainder of the paper is organized as follows. For the spray, soot, and radiation models, Sec. 2 describes the mathematical formulation. Section 3 describes the computational methods for implementing the spray, soot, and radiation models and coupling them with the block-structured gas phase solver. Section 4 describes the model verification using comparisons with previous experiments and numerical results. Section 5 presents parallel performance benchmarks for the codes on multiple supercomputers, as well as performance gains from using CPU/GPU heterogeneous architectures. Section 6 describes three production simulations that incorporate PeleMP models in PeleLMeX: sooting ethylene-air laminar coflow flame and turbulent jet flame with radiation heat loss performed on Frontier, and bluff-body swirl stabilized spray flames with SAF in an aero-engine relevant laboratory scale burner on Perlmutter GPUs at the National Energy Research Scientific

Computing Center (NERSC). Lastly, Sec. 7 provides a summary and future scientific outlook of the exascale combustion simulation capabilities.

2 Mathematical Formulation

In this section, the mathematical formulation of the dilute spray droplet, soot, and radiation models is presented in the context of compressible and low-Mach finite volume solvers, PeleC and PeleLMeX. The governing equations for these solvers are first presented to provide context for their coupling with the multiphysics models.

The compressible gas phase conservation equations for mass, species continuity, momentum, and total energy in PeleC are given as

$$\frac{\partial \rho}{\partial t} + \nabla \cdot \rho \mathbf{u} = S_\rho \tag{1}$$

$$\frac{\partial \rho Y_n}{\partial t} + \nabla \cdot \rho Y_n \mathbf{u} = -\nabla \cdot \mathcal{F}_n + \rho \dot{\omega}_n + S_{\rho Y_n}, \forall n \in N_s \tag{2}$$

$$\frac{\partial \rho \mathbf{u}}{\partial t} + \nabla \cdot (\rho \mathbf{u} \otimes \mathbf{u} + \Pi) = -\nabla p + S_{\rho \mathbf{u}} \tag{3}$$

$$\frac{\partial \rho E}{\partial t} + \nabla \cdot (\rho \mathbf{u} E + p \mathbf{u}) = \nabla \cdot \mathcal{Q} - \nabla \cdot (\Pi \cdot \mathbf{u}) + S_{\rho E} \tag{4}$$

where ρ is the density, $\mathbf{u}$ is the velocity vector, p is the pressure, Y is the mass fraction, N_s is the number of species, and E is the total specific energy

$$E = |\mathbf{u}|^2/2 + \sum_{n=0}^{N_s} Y_n h_n(T) - p/\rho$$

Additionally, $h_n(T)$ is the enthalpy of species n at temperature T, $\mathcal{F}_n$ is the species transport fluxes, $\dot{\omega}_n$ is the chemical reaction source term, Π is the viscous stress tensor, and $\mathcal{Q}$ is the diffusive heat flux. The terms with S in each equation are the source terms and represent the coupling of the soot, spray, and radiation models with the gas phase.

The conservation equations for PeleLMeX are the same as Eqs. (1)–(3). The energy equation, Eq. (4), is replaced with

$$\frac{\partial \rho h}{\partial t} + \nabla \cdot \rho h \mathbf{u} = \nabla \cdot \mathcal{Q} + S_{\rho h} \tag{5}$$

Additionally, the low-Mach formulation requires that the solution evolve subject to a constraint on the divergence of velocity

$$\begin{aligned}
\nabla \cdot \mathbf{u} = &\frac{1}{\rho c_p T}\left(\nabla \cdot \lambda \nabla T + \sum_n h_n \nabla \cdot \mathcal{F}_n - \nabla \cdot h_n \mathcal{F}_n\right) \\
&- \frac{\bar{M}}{\rho}\sum_n \frac{\nabla \cdot \mathcal{F}_n}{M_n} + \frac{1}{\rho}\sum_n \left(\frac{\bar{M}}{M_n} - \frac{h_n}{c_p T}\right)\dot{\omega}_n \\
&+ \frac{\bar{M}}{\rho}\sum_n \frac{S_{\rho Y_n}}{M_n} + \frac{1}{\rho c_p T}\left(S_{\rho h} - \sum_n h_n S_{\rho Y_n}\right) \\
\equiv & S_{\text{div}} .
\end{aligned} \tag{6}$$

where M_n is the molar mass, $\bar{M}$ is the average molar mass of a mixture, $\mathcal{R}$ is the universal gas constant, c_p is the specific heat at constant pressure, and λ is the thermal conductivity. This constraint arises by setting the total derivative of the thermodynamic pressure to zero (indicating the lack of acoustic propagation), expanding the pressure dependencies with the chain rule, substituting the conservation equations, and noting that $h = \sum_n Y_n h_n$.

2.1 Spray Droplet Modeling. The fuel spray is described as a collection of Lagrangian particles, representing point-like fuel droplets dispersed in the Eulerian gas phase. The Eulerian–Lagrangian coupling described in this Section has been shown to capture the relevant spray characteristics (such as liquid/vapor penetration and droplet/gas velocity fields) as long as the gas-parcel interactions are carefully calibrated in relation to the computational mesh and the near-injection properties of the spray are known [12]. In the simulation of direct injection (DI) in internal combustion engines, Eulerian–Lagrangian coupling [13] can capture the unsteady behavior (for instance, cyclic variations) that is considered responsible for misfire and knocking [14,15]. Essentially, the same computational framework has been adopted in combustion modeling of aviation gas turbines, with recent studies examining the performance of alternative jet fuels at conditions close to blowout [16]. In either of these application spaces, PeleMP, as for all of its predecessors, relies on external information concerning the spray characteristics close to the injector. The process of liquid jet disintegration, caused (typically) by turbulence interaction, is not included because it is topologically complex [17], is ultimately caused by pinch-off dynamics at submicron scales [18], and is often affected by specific injector hardware details [19].

The spray droplet modeling in PeleMP relies on the following assumptions: dilute spray, that is, the droplet volume inside an Eulerian cell is much smaller than the volume of the gas phase; the droplets can be modeled as Lagrangian point source terms relative to the Eulerian gas phase; infinite conductivity model, that is, the temperature within a droplet is temporally varying but spatially uniform; ideal equilibrium, that is, the liquid and vapor state at the surface of the droplet are in equilibrium; and radiation, Soret, and Dufour effects are neglected in regards to the spray modeling. The evaporation model is based on work by Abramzon and Sirignano [20], and the multicomponent evaporation is based on work by Tonini [21].

The subscript notation adopted in this section is as follows: d relates to the liquid droplet, v relates to the vapor state that is in equilibrium with the liquid and gas phase, L relates to the liquid phase, and g relates to the gas phase. The subscript r relates to the reference state with which to approximate the thermophysical and transport properties. This reference state is assumed to be in the evaporating film that surrounds the droplet state and is approximated as

$$T_r = T_d + A(T_g - T_d) \tag{7}$$

$$Y_{r,n} = Y_{v,n} + A(Y_{g,n} - Y_{v,n}) \tag{8}$$

where $A = 1/3$ according to the one-third rule [22].

The user is required to provide a reference temperature for the liquid properties, T^*, the critical temperature for each liquid species, $T_{c,n}$, the boiling temperature for each liquid species at atmospheric pressure, $T^*_{b,n}$, the latent heat at T^*, $h_{L,n}(T^*)$, and the liquid specific heat at T^*, $c_{p,L,n}(T^*)$. This reference temperature is a constant value and is not related to the reference state denoted by the subscript r.

The Lagrangian droplet is governed by a set of differential equations to model the location, mass, mass fraction, momentum, and energy

$$\frac{d\mathbf{X}_d}{dt} = \mathbf{u}_d \tag{9}$$

$$\frac{dm_d}{dt} = \sum_{n=0}^{N_L} \dot{m}_n \tag{10}$$

$$m_d \frac{dY_{d,n}}{dt} = \dot{m}_n - Y_{d,n} \frac{dm_d}{dt} \tag{11}$$

$$m_d \frac{d\mathbf{u}_d}{dt} = \mathbf{F}_d + m_d \mathbf{g} \tag{12}$$

$$m_d c_{p,L} \frac{dT_d}{dt} = \sum_{n=0}^{N_L} \dot{m}_n h_{L,n}(T_d) + \mathcal{Q}_d \tag{13}$$

where $\mathbf{X}_d$ is the droplet location vector in physical space, $\mathbf{u}_d$ is the droplet velocity vector, N_L is the number of liquid species, and m_d is the droplet mass. Droplets are assumed to be spherically symmetric, so the mass can be computed based on the diameter, d_d, using

$$m_d = \frac{\pi}{6} \rho_d(T_d) d_d^3$$

and the liquid density is

$$\rho_d = \left(\sum_{n=0}^{N_L} \frac{Y_{d,n}}{\rho_{L,n}} \right)^{-1}$$

The procedure for computing the time advancement of a droplet is as follows:

(1) Interpolate the gas phase values at the droplet location.
(2) Compute the boiling temperature for species n at the current gas phase pressure using the Clasius–Clapeyron relation

$$T_{b,n} = \left(\log\left(\frac{p_{\text{atm}}}{p_g} \right) \frac{\mathcal{R}}{M_n h_{L,n}(T^*_{b,n})} + \frac{1}{T^*_{b,n}} \right)$$

Since we only have the latent heat at the reference condition temperature, we estimate the enthalpy at the boiling condition using Watson's law.

(3) Compute the latent heat of the droplet using [23]

$$h_{L,n}(T_d) = h_{g,n}(T_d) - h_{g,n}(T^*) + h_{L,n}(T^*) - c_{p,L,n}(T^*)(T_d - T^*)$$

and the saturation pressure, $p_{\text{sat},n}$, using either the Clasius–Clapeyron relation or the Antoine curve fit.

(4) Estimate the mass fractions in the vapor state using Raoult's law

$$Y_{v,n} = \frac{\chi_{v,n} M_n}{\bar{M}_v + \bar{M}_g(1 - \chi_{v,\text{sum}})} \quad \forall n \in N_L,$$

$$\chi_{v,\text{sum}} = \sum_{n=0}^{N_L} \chi_{v,n},$$

$$\chi_{v,n} = \frac{\chi_{d,n} p_{\text{sat},n}}{p_g},$$

$$\chi_{d,n} = \frac{Y_{d,n}}{M_n} \left(\sum_{k=0}^{N_L} \frac{Y_{d,k}}{M_k} \right)^{-1},$$

$$\bar{M}_v = \sum_{n=0}^{N_L} \chi_{v,n} M_n,$$

where χ is the molar fraction. If $\chi_{g,n} p_g > p_{\text{sat},n}$, then $\chi_{v,n} = Y_{v,n} = 0$ for that particular species in the equations above, since that means the gas phase is saturated. The mass fractions in the reference state for the fuel are computed using the one-third rule, and the remaining reference mass fractions are normalized gas phase mass fractions to ensure they sum to unity

$$Y_{r,n} = \begin{cases} Y_{v,n} + A(Y_{g,n} - Y_{v,n}) & \text{If } Y_{v,n} > 0, \\[2ex] \dfrac{1 - \displaystyle\sum_{k=0}^{N_L} Y_{v,k}}{1 - \displaystyle\sum_{k=0}^{N_L} Y_{g,k}} Y_{g,n} & \text{Otherwise.} \end{cases} \quad \forall n \in N_s$$

(5) The average molar mass, specific heat, and density of the reference state in the gas film are computed as

$$\bar{M}_r = \left(\sum_{n=0}^{N_s} \frac{Y_{r,n}}{M_n} \right)^{-1},$$

$$c_{p,r} = \sum_{n=0}^{N_s} Y_{s,n} c_{p,g,n}(T_r),$$

$$\rho_r = \frac{\bar{M}_r p_g}{\mathcal{R} T_r}.$$

(6) Transport properties are computed using the reference state: dynamic viscosity, μ_r, thermal conductivity, λ_r, and mass diffusion coefficient for species n, $D_{r,n}$. These values are provided by the PelePhysics library. It is important to note that PelePhysics provides a mixture averaged mass diffusion coefficient $(\rho D)_{r,n}$, which is converted into the binary mass diffusion coefficient using $(\rho D)_{r,n} = (\rho D)_{r,n} \bar{M}_r / M_n$. The mass diffusion coefficient is then normalized by the total fuel vapor molar fraction

$$(\rho D)_{r,n}^* = \frac{\chi_{v,n}(\rho D)_{r,n}}{\chi_{v,\text{sum}}} \ \forall n \in N_L$$

and a total of

$$(\rho D)_r = \sum_{n=0}^{N_L} (\rho D)_{r,n}^*$$

(7) The momentum source is a function of the drag force

$$\mathbf{F}_d = \frac{1}{2} \rho_r C_D A_d ||\Delta \mathbf{u}|| \Delta \mathbf{u}$$

where $\Delta \mathbf{u} = \mathbf{u}_g - \mathbf{u}_d$, $A_d = \pi d_d^2/4$ is the frontal area of the droplet, and C_D is the drag coefficient for a sphere, which is estimated using the standard drag curve for an immersed sphere

$$C_D = \frac{24}{\text{Re}_d} \begin{cases} 1 & \text{If } \text{Re}_d < 1, \\ 1 + \dfrac{\text{Re}_d^{2/3}}{6} & \text{Otherwise.} \end{cases}$$

The droplet Reynolds number is defined as $\text{Re}_d = \rho_r d_d ||\Delta \mathbf{u}|| / \mu_r$.

(1) The mass source term is modeled according to Abramzon and Sirignano [20]. The following nondimensional numbers and factors are used

$$F(B) = (1+B)^{0.7} \frac{\log(1+B)}{B},$$

$$F_2 = \max\left(1, \min\left(400, \text{Re}_d\right)^{0.077}\right),$$

$$\text{Sh}_0 = 1 + (1 + \text{Re}_d \text{Sc}_r)^{1/3} F_2,$$

$$\text{Nu}_0 = 1 + (1 + \text{Re}_d \text{Pr}_r)^{1/3} F_2,$$

$$\text{Sh}^* = 2 + \frac{\text{Sh}_0 - 2}{F(B_M)},$$

$$\text{Nu}^* = 2 + \frac{\text{Nu}_0 - 2}{F(B_T)}$$

where $\text{Pr}_r = \mu_r c_{p,r} / \lambda_r$ and $\text{Sc}_r = \mu_r / (\rho D)_r$. The Spalding numbers for mass transfer, B_M, and heat transfer, B_T, are computed using

$$B_M = \frac{\displaystyle\sum_{n=0}^{N_L} Y_{v,n} - \sum_{n=0}^{N_L} Y_{g,n}}{1 - \displaystyle\sum_{n=0}^{N_L} Y_{v,n}},$$

$$B_T = (1 + B_M)^{\phi} - 1,$$

where

$$\phi = \frac{c_{p,r}(\rho D)_r \text{Sh}^*}{\lambda_r \text{Nu}^*}$$

Note the dependence of Nu^* on B_T such that an iterative scheme is required to solve for both. The droplet vaporization rate and heat transfer become

$$\dot{m}_n = -\pi(\rho D)_{r,n}^* d_d \text{Sh}^* \log(1 + B_M) \ \forall n \in N_L,$$

$$\mathcal{Q}_d = \pi \lambda_r d_d (T_g - T_d) \text{Nu}^* \frac{\log(1 + B_T)}{B_T}.$$

If the gas phase is saturated for all liquid species, the equations for heat and mass transfer become

$$\dot{m}_n = 0,$$

$$\mathcal{Q}_d = \pi \lambda_r d_d (T_g - T_d) \text{Nu}_0.$$

(1) To alleviate conservation issues at AMR interfaces, each parcel only contributes to the gas phase source term of the cell containing it. The gas phase source terms for a single parcel to the cell are

$$S_\rho = \mathcal{C} \sum_{n=0}^{N_L} \dot{m}_n,$$

$$S_{\rho Y_n} = \mathcal{C} \dot{m}_n,$$

$$\mathbf{S}_{\rho \mathbf{u}} = \mathcal{C} \mathbf{F}_d,$$

$$S_{\rho h} = \mathcal{C} \left(\mathcal{Q}_d + \sum_{n=0}^{N_L} \dot{m}_n h_{g,n}(T_d) \right),$$

$$S_{\rho E} = S_{\rho h} + \frac{1}{2} ||\mathbf{u}_d|| S_\rho + \mathcal{C} \mathbf{F}_d \cdot \mathbf{u}_d,$$

where $\mathcal{C} = -N_d/V_{\text{cell}}$, N_d is the number of droplets per computational parcel, and V_{cell} is the volume for the cell of interest. Note that the cell volume can vary depending on the AMR level and if an embedded boundary (EB) is present in the cell.

Additionally, the Kelvin-Helmholtz Rayleigh-Taylor (KHRT) breakup model proposed by Lui et al. [24] is implemented in PeleMP. For the sake of brevity, details regarding the KHRT implementation into PeleMP are not provided in the present study.

2.2 Soot Modeling. In PeleMP, soot formation, growth, and oxidation is modeled using the Hybrid Method of Moments (HMOM) developed by Mueller et al. [10]. This approach combines the numerical ease of the method of moments with interpolative closure (MOMIC) with the ability to capture the bimodal nature of the soot number density function (NDF) provided by the direct quadrature method of moments (DQMOM). The soot model considers two quantities to describe the fractal aggregate morphology of soot [25]: the particle volume V and particle surface area S. Bivariate moments $M_{x,y}$ of the soot NDF, where x is the order for volume and y for surface area, are evolved to describe the soot population. Additionally, HMOM also evolves the number density of incipient soot particles N_0 of size V_0 and S_0 (assuming spherical incipient soot particles). To provide closure in the moment source terms, unknown moments are determined from an expression that combines the polynomial interpolation of MOMIC for the larger particles with a quadrature node for the smaller, incipient particles

$$M_{x,y} = N_0 V_0^x S_0^y + \exp\left(\sum_{r=0}^{R} \sum_{k=0}^{r} a_{r,k} x^k y^{r-k} \right) \tag{14}$$

where R is the order of the polynomial interpolation and $a_{r,k}$ are the polynomial interpolation coefficients. In the results shown in this

paper, first-order polynomial interpolation of the moments ($R = 1$) is used, so the above equation reduces to

$$M_{x,y} = N_0 V_0^x S_0^y + N_L V_L^x S_L^y \tag{15}$$

where N_L, V_L, and S_L are the number density, mean volume, and mean surface area of the larger particles, respectively. As a result, four transport equations are solved: $M_{0,0}$ (total number density), $M_{1,0}$ (volume fraction, also denoted as f_v), $M_{0,1}$, and N_0.

The governing equations for the soot moments are

$$\frac{\partial M_{x,y}}{\partial t} + \nabla \cdot M_{x,y} \mathbf{u} = -\nabla \cdot \boldsymbol{J}_M + \dot{M}_{x,y} \tag{16}$$

where $\boldsymbol{J}_M$ is the soot mass flux and $\dot{M}_{x,y}$ is the soot source term. The current formulation ignores both molecular diffusion and thermophoretic effects, making the first term of the right-hand side zero. The moment source terms include contributions from nucleation (from two polycyclic aromatic hydrocarbon (PAH) dimers), condensation, coagulation, surface growth, surface oxidation, and fragmentation. Complete details on the formulation of these source terms can be found in the work of Mueller et al. [10,26].

The soot model couples with the gas phase through species concentration, $S_{\rho Y_n}$, and energy/enthalpy source terms, $S_{\rho E}/S_{\rho h}$. Specifically, nucleation and condensation remove PAH species mass from the gas-phase to create new and grow soot particles, and surface growth and surface oxidation reactions cause O, O_2, H, H_2, H_2O, OH, CO, and C_2H_2 to be added or subtracted from the gas phase to the soot variables.

2.3 Radiation Modeling. Thermal radiation plays a vital role in the overall heat transfer of hydrocarbon flames [27]. This significance arises from the fact that the radiative energy emitted from the combustion products is proportional to differences in the fourth power of temperature. Radiative transfer in an absorbing, emitting, and scattering medium can be formulated by considering conservation of radiative energy, known as the radiative transfer equation (RTE), which is an integro-differential equation with spatial and directional dependency

$$\hat{\mathbf{s}} \cdot \nabla_\tau I_\eta + I_\eta = (1 - \omega_\eta) I_{b\eta} + \frac{\omega_\eta}{4\pi} \int_{4\pi} I_\eta(\hat{\mathbf{s}}') \Phi_\eta(\hat{\mathbf{s}} \cdot \hat{\mathbf{s}}') d\Omega' \tag{17}$$

where $I_\eta(\tau, \hat{\mathbf{s}})$ is the spectral radiative intensity, which is defined as the spectral radiative energy flow per unit solid angle and unit area normal to the photon rays; $\tau = \int \beta_\eta d\mathbf{r}$ is an optical coordinate and β_η is the spectral extinction coefficient, which is the sum of spectral absorption coefficients κ_η and scattering coefficients $\sigma_{s\eta}$; $I_{b\eta}$ is the blackbody intensity or Planck function; $\omega_\eta = \sigma_{s\eta}/\beta_\eta$ is the spectral scattering albedo; and $\Phi_\eta(\hat{\mathbf{s}} \cdot \hat{\mathbf{s}}')$ is the scattering phase function. The RTE mathematically describes augmentation and extinction of spectral intensity along a path in the direction of $\hat{\mathbf{s}}$.

The net energy balance at any location in the medium is obtained by integrating the spectral intensity over all directions and wavenumbers. The net radiative heat source, $S_{\rm rad}$, is the difference between local absorption, $S_{\rm abs}$, and emission, $S_{\rm emi}$, and expands to,

$$S_{\rm rad} = -\nabla \cdot \mathbf{q}_{\rm rad} = -(S_{\rm emi} - S_{\rm abs}) = -4\kappa_P \sigma T^4 + \int_0^\infty \kappa_\eta G_\eta d\eta \tag{18}$$

$$G_\eta = \int_{4\pi} I_\eta(\tau, \hat{\mathbf{s}}) d\Omega \tag{19}$$

where the spectral incident radiation, G_η, is defined as the directional integral of spectral radiative intensity.

The gaseous products of a hydrocarbon flame mostly radiate and absorb across certain bands in the infrared spectrum, while soot, if present, usually dominates over gas radiation. Experiments under atmospheric pressure have shown that soot emission in most cases is much stronger than gas emission. Although the radiative properties of soot materials are also functions of wavelength, usually the gray approximation for soot is fairly good for most combustion conditions. The gray model uses a single mean absorption coefficient, usually the Planck-mean absorption coefficient κ_P, for radiation calculations. κ_P is calculated by weighing the spectral absorption coefficient κ_η with the Planck function $I_{b\eta}$

$$\kappa_P = \frac{\int_0^\infty I_{b\eta} \kappa_\eta d\eta}{\int_0^\infty I_{b\eta} d\eta} = \frac{\pi}{\sigma T^4} \int_0^\infty I_{b\eta} \kappa_\eta d\eta \tag{20}$$

When the gray model is used, Eq. (18) is reduced to

$$S_{\rm rad} = -\kappa_P(4\sigma T^4 - G) \tag{21}$$

The soot radiation model assumes the soot particles are spherical and small (at 10^1–10^2 nm scale) so that Rayleigh's theory can be applied. The radiative property of soot depends on the complex index of refraction, which is defined as

$$m_\lambda = n_\lambda - ik_\lambda \tag{22}$$

The correlations of n_λ and k_λ with the wavelength λ (in μm) are based on experiments Charalampopoulos et al. [28]

$$n_\lambda = 1.811 + 0.1263(\ln \lambda) + 0.0270(\ln \lambda)^2 + 0.0417(\ln \lambda)^3 \tag{23}$$

$$k_\lambda = 0.5821 + 0.1213(\ln \lambda) + 0.2309(\ln \lambda)^2 - 0.0100(\ln \lambda)^3 \tag{24}$$

With the spectral complex refractive index, the spectral absorption coefficient is calculated by

$$\kappa_\lambda = \frac{36\pi n_\lambda k_\lambda}{\left(n_\lambda^2 - k_\lambda^2 + 2\right)^2 + 4n_\lambda^2 k_\lambda^2} \frac{f_v}{\lambda} \tag{25}$$

where f_v is the soot volume fraction.

The P1 method is used as the RTE solver in this study. The P1 method is the first-order spherical harmonics approximation [11] of the angular distribution of the radiative intensity. With the P1 approximation, Eq. (17) is converted to

$$\frac{1}{3\kappa} \nabla \cdot \left(\frac{1}{\beta} \nabla G\right) - G = -4\pi I_b \tag{26}$$

The corresponding Marshak's boundary condition for G at $\mathbf{r} = \mathbf{r}_w$ is

$$-\frac{2-\varepsilon}{\varepsilon} \frac{2}{3\beta} \hat{\mathbf{n}} \cdot \nabla G + G = 4\pi I_{bw} \tag{27}$$

where ϵ is the surface emittance and I_{bw} is the blackbody radiative intensity from the wall. The P1 equation is a Helmholtz equation with Robin-type boundary condition. It is solved by the multigrid (MG) method in this study.

Radiation is coupled to the reacting gas phase flow through the energy equation, which is, Eq. (4) for the compressible formulation as in PeleC, and Eq. (5) for the low-Mach formulation as in PeleLMeX. The radiative heat source term $S_{\rm rad}$ is added to the right-hand side of the energy equation, as part of $S_{\rho E}$ or $S_{\rho h}$.

3 Computational Methods

The Pele suite of codes, including PeleMP, utilizes the AMReX library [6]. AMReX is a framework for massively parallel, block-structured applications that use AMR. The functionality and data

structures provided by AMReX are too numerous to list here, but some notable aspects include patch-based data structures with memory management/exchange routines, distribution mapping for parallel performance, GPU kernel launch abstraction for improved portability, EB capabilities, and particle structures and routines.

3.1 Time Marching. In this section, we will refer to U^n to be the solution state at time t^n, A is the advection source term data, D is the diffusion source term data, S_{ext} is the external source term data (for sprays, soot, and radiation), and u is the velocity data.

Figure 1 is a summary of the spectral deferred correction (SDC) time-step procedure in PeleC with the external source terms for spray, soot, and radiation. SDC time stepping allows for larger time-step sizes while ensuring the stiff processes remain coupled. The SDC iterations are denoted by the index k, and the upper green box shows the steps that occur only during the first SDC iteration ($k = 0$). The lower box shows the steps that occur for every SDC iteration. The advective forcing, $A^{n+1/2}$, is a function of the most recently computed external source terms, S_{ext}^*, as well as the states U^n and $U^{n+1,k-1}$. The updated diffusion source term uses the original state, U^n, and the most recently computed external source term $S_{\text{ext}}^{\text{new}}$. The implicit chemistry integration and state update use all of the most recently computed source terms and the state U^n.

Figure 2 is a summary of the SDC time-step procedure in PeleLMeX. In contrast to PeleC, the external source terms are only computed once per time-step during the initial SDC iteration ($k = 0$) and used throughout the time advancement. The velocity prediction and solve are functions of the external momentum source terms, and the divergence constraint from Eq. (6), advection solves, and chemistry integration are functions of all external source terms. Steps that require a linear solution are denoted.

3.2 Spray Modeling. Spray droplets in PeleMP are modeled as computational parcels which are contained in a C++ class denominated as `SprayParticleContainer`. This class is inherited from the `AmrParticleContainer` class in the AMReX library [6]. The AMReX particle library provides many different features, including particle memory management, redistribution, IO, tiling, iterating, and much more. AMReX particles inherently contain the particle position in space (stored as doubles), the CPU number the particle was generated on, and the particle ID; the last two are stored as integers. In addition to these components, PeleMP spray particles contain component data for velocity, diameter, temperature, and mass fractions. PeleMP spray particle component data is stored in the Arrays-of-Structs style, meaning all components associated with a single particle are adjacent in memory, followed by all components for another particle. This differs from Structs-of-Arrays style, where data for a single component for all particles are grouped in memory.

Particles are stored in memory based on the patch in which the particle spatially resides in the domain. If a particle moves from one patch to another during an update, a `Redistribute` routine must be called. This routine can become expensive as it involves device-to-host and internodal communication. The spray particle update routine, `updateParticles`, consists of two nested loops: the outer loop is over the patches associated with the Eulerian mesh that contain particles, this is called a `ParIter` loop, and the inner loop is over the particles that are physically located within that patch. When GPU hardware is used, the inner loop is a GPU kernel launch.

Solving the fully coupled spray modeling equations requires specific handling of the Lagrangian particles. Particular care must be taken during particle creation, particle-mesh and particle-boundary interactions, and particle redistribution to ensure solution consistency and minimize performance degradation.

3.2.1 Particle Handling for Adaptive Mesh Refinement. A number of steps are taken to ensure consistent particle-mesh interactions for refined grids. First, we will define three types of particles: Active, Ghost, and Virtual. Active particles exist at the most refined mesh level for the particle location; these particles

persist throughout the entire simulation, unless they evaporate or leave the domain. Ghost particles exist on finer levels and represent active particles that are on coarser levels and adjacent to an AMR interface; these are necessary to account for particles that might move onto the finer level during a time-step. Virtual particles exist on coarser levels and represent active particles that are on finer levels; these are necessary for coarser levels to be aware of contributions from particles when subcycling occurs or when a fine particle moves off of a fine level to a coarse level during a time-step. A demonstration of a refined mesh with two Active particles is shown in Fig. 3. The lines represent cells on the mesh; the thicker lines represent the AMR interface between the levels; and the black dots represent Active particles on the fine and coarse levels adjacent to an AMR interface. AMReX uses patch-based refinement, meaning refined cells are overlaid on coarser cells but do not replace the coarser cells; this is demonstrated in Fig. 4, where the refined level is extruded above the coarse level. In the figure, two active particles (top-left and bottom-right), a ghost particle (top-right), and a virtual particle (bottom-left) are indicated.

If a particle convects outside of a domain boundary or EB, logic in PeleMP ensures the particle is handled properly. Specifically, if the particle moves outside of a nonreflecting domain boundary (like an outflow boundary), the particle ID is set to -1, ensuring that particle is deleted during next redistribute routine. The particle is reflected back into the domain if it moves outside of a reflecting boundary (such as a wall or EB face).

3.2.2 Spray Time Marching. A particle time-step is used as a limiting factor for the determination of the gas phase time-step size, computed as

$$\Delta t_{\text{spray}} = \frac{\Delta x \text{CFL}_{\text{spray}}}{\max(\mathbf{u}_d)}$$

where $\text{CFL}_{\text{spray}}$ is the spray CFL number, which determines how many cells a particle can travel over a time-step, and $\max(\mathbf{u}_d)$ is the maximum velocity of all particles. Time advancement for spray particles differs depending on which gas phase solver is being used, PeleC or PeleLMeX. PeleC uses subcycling, meaning the finer level solution advances multiple smaller time steps relative to the coarser level. The time-step size and number of time steps depend on the refinement ratio between the levels. For example, for a refinement ratio of two, cells on the fine level will advance two steps at half the time-step size relative to a single step on the coarse level. For subcycling solutions, $\text{CFL}_{\text{spray}} \leq 0.5$ due to the increased logistical considerations necessary. In contrast, PeleLMeX does not use subcycling, meaning all levels are advanced simultaneously at a single time-step size. Because of this, all spray particles and corresponding gas phase source terms are updated once during the initial SDC iteration.

Figure 1 shows how spray source terms are part of the SDC iteration for PeleC. However, there are a few distinctions that are not part of the diagram. Specifically, there are two different particle update routines when coupled with PeleC, `MoveKickDrift`, and `MoveKick`. This procedure is based on the kick-drift-kick sequence outlined by Miniati and Colella [29] which ensures the integral of motion will be conserved on average. More information is provided by Quinn et al. [30]. `MoveKickDrift`: updates the mass fractions, temperature, diameter, and velocity of the liquid droplet from time t to $t + \Delta t/2$; computes the gas phase source terms ($S_{\text{ext}}^{\text{old}}$ step in Fig. 1) for mass, momentum, and energy from time t to $t + \Delta t/2$; and updates the particle position to time $t + \Delta t$. The spray source terms for this step are deposited in the cell containing the particle at time t. As Figure 1 shows, this source term is used to compute the intermediate state during the SDC updates. `MoveKick`: updates the mass fractions, temperature, diameter, and velocity of the liquid droplets and computes the gas phase source terms ($S_{\text{ext}}^{\text{new}}$ step in Fig. 1) from time $t + \Delta t/2$ to $t + \Delta t$. This operation only occurs during the final SDC iteration ($k = k_{\text{max}} - 1$). The spray source terms are deposited in the cell containing the particle at time $t + \Delta t$.
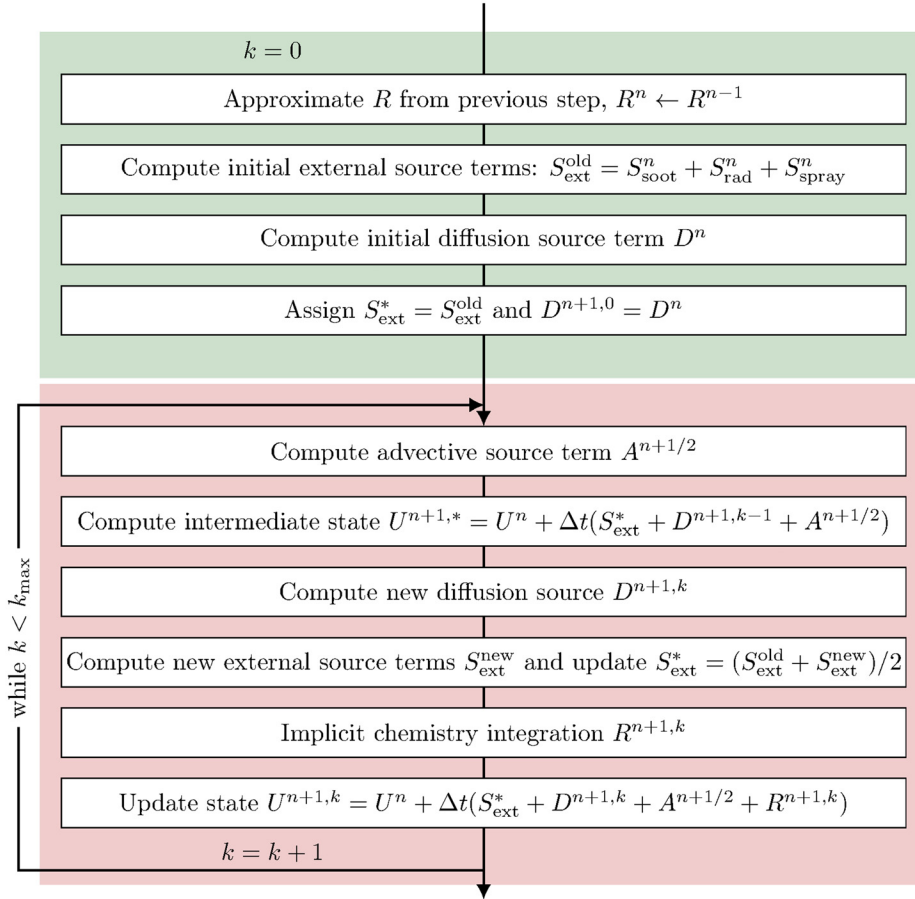
Fig. 1   Algorithm diagram showing the PeleC SDC time advancement

In general, the spray update on level ℓ in PeleC is as follows:

(1) During the first SDC iteration:
  (a) Active and Virtual particles on level $\ell + 1$ are used to create Virtual particles on level ℓ.
  (b) Active particles on level $\ell - 1$ near AMR interfaces are used to create Ghost particles on level ℓ.
  (c) `MoveKickDrift` the Active, Virtual, and Ghost particles.

After the SDC iterations are finished, perform the `post_timestep` operations. Virtual particles are deleted. If it is the final sub-cycle on a refined level, the Ghost particles are deleted and a redistribution is performed for all Active particles on level ℓ and above.

In the current implementation, the same grid distributions are used for the particles and gas phase. This has the potential for load balancing when particles are concentrated in only specific parts of the grid, which is the case for most spray injection cases. Future work will utilize the "dual-grid" method in AMReX, which allows for different load-balancing strategies to be used for mesh and particle work.

3.3   Radiation Solver. At each time-step, the scalar fields ($\mathbf{Y}_g$, T_g, P_g) and soot volume fraction (f_v), are passed to the radiation module to evaluate the radiative properties (κ and I_b). Next, the P1 equation, Eq. (26), is solved by either the native AMReX linear solvers or other compatible external solvers, such as Hypre [31] or PETSc [32], etc. For the results shown in this study, the native AMReX multigrid solver [33] is used with the BICGStab as the bottom solver. When coupling to PeleC, which requires subcycling in time, the radiation equation is solved at each AMR level. In this case, the solution follows the regular single-level multigrid V-cycle or F-cycle procedures. When coupling to PeleLMeX, with no subcycling needed, all the AMR levels need to be solved in a composite manner. This multilevel multigrid composite solution approach is realized by integrating the refined AMR levels into the multigrid level hierarchy. More details of the AMReX native linear solvers are described in Refs. [6] and [34].

The AMReX linear solver solves an elliptic equation in the canonical form

$$\alpha\psi - \nabla \cdot \gamma\nabla\psi = f \qquad (28)$$

where ψ is the unknown to solve; α and γ are the coefficient fields; and f is the source term. Correspondingly, for the P1 equation, $\alpha = \kappa$, $\gamma = 1/(3\beta)$, and $f = 4\pi\kappa I_b$. Physical boundary conditions are applied to the coarsest AMR level, while for the finer levels, the boundary conditions are Dirichlet type from the coarser level. The Robin-type boundary can be generalized as.

$$a\psi + b\nabla_n\psi = c \qquad (29)$$

The Marshak's boundary condition specifies the coefficients as $a = \beta$, $b = -2(2 - \varepsilon)/3\varepsilon$, $c = 4\pi\beta I_{bw}$.

The discretization of the governing equation, Eq. (28), in 1-D gives

$$\alpha_i\psi_i + \frac{\left(\gamma\frac{d\psi}{dx}\right)_{i-1/2} - \left(\gamma\frac{d\psi}{dx}\right)_{i+1/2}}{h} = f_i \qquad (30)$$

In a cell-centered formulation, the subscript i denotes the index of the cell, and $i\pm1/2$ denote the cell faces. If i is the index of a boundary cell at the right boundary, $i + 1/2$ denotes the right boundary face. At the boundary face, the Robin-type boundary, Eq. (29), is discretized as
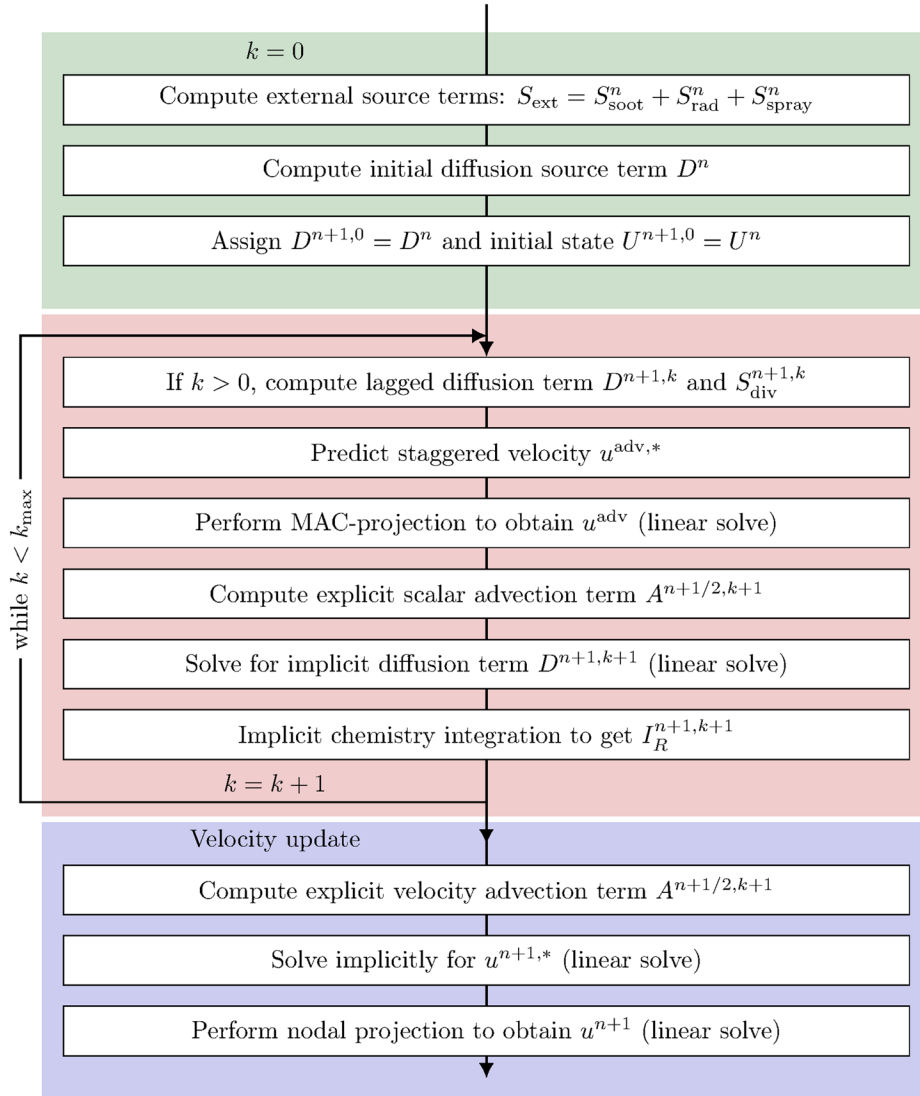
$k = 0$

Compute external source terms: $S_{\text{ext}} = S_{\text{soot}}^n + S_{\text{rad}}^n + S_{\text{spray}}^n$

Compute initial diffusion source term D^n

Assign $D^{n+1,0} = D^n$ and initial state $U^{n+1,0} = U^n$

while $k < k_{\max}$

If $k > 0$, compute lagged diffusion term $D^{n+1,k}$ and $S_{\text{div}}^{n+1,k}$

Predict staggered velocity $u^{\text{adv},*}$

Perform MAC-projection to obtain u^{adv} (linear solve)

Compute explicit scalar advection term $A^{n+1/2,k+1}$

Solve for implicit diffusion term $D^{n+1,k+1}$ (linear solve)

Implicit chemistry integration to get $I_R^{n+1,k+1}$

$k = k + 1$

Velocity update

Compute explicit velocity advection term $A^{n+1/2,k+1}$

Solve implicitly for $u^{n+1,*}$ (linear solve)

Perform nodal projection to obtain u^{n+1} (linear solve)

Fig. 2   Algorithm diagram showing the PeleLMeX SDC time advancement

$$a \frac{\psi_i + \psi_{i+1}}{2} + b \frac{\psi_{i+1} - \psi_i}{h} = c \qquad (31)$$

which gives the flux at the boundary face $i + 1/2$ in Eq. (30)

$$\left(\frac{d\psi}{dx}\right)_{i+1/2} = \frac{\psi_{i+1} - \psi_i}{h} \qquad (32)$$
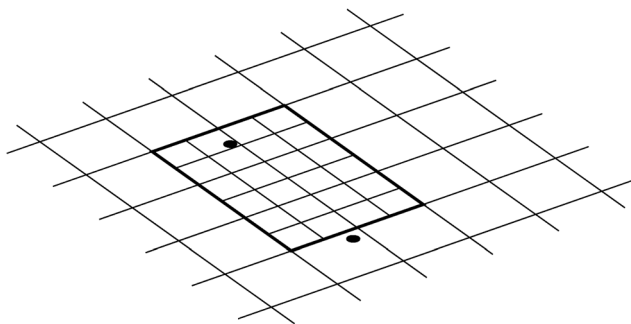
Fig. 3   Demonstration of two particles on a refined mesh
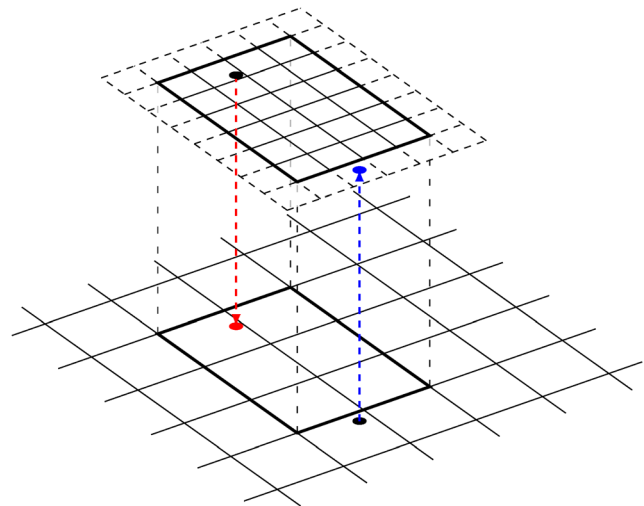
Fig. 4   Demonstration of different particle types relative to a refined mesh, represented as the dots: active (top-left and bottom-right), ghost (top-right), and virtual (bottom-left)

4 Verification

In this section, we provide verification for the spray, soot, and radiation model implementation using comparisons with both experimental and numerical results from the literature. The spray model implementation is verified through single droplet tests and a diesel spray injection case. The radiation and soot model implementations are verified using the method of manufacturing solutions (MMS) and with a 1D premixed burner-stabilized flame.

4.1 Single Droplet. Three different single droplet cases from the literature are presented as validation of the droplet evaporation models. The parameters and corresponding references are shown in Table 1. The gas phase is air traveling at the listed velocity with the particle fixed in the center of the domain, except for case 1, where air is quiescent and the droplet is given an initial velocity of 15 m/s. The liquid mass fractions for each case are: pure n-Decane, 0.5 n-Decane and 0.5 n-Octane, and 0.33 n-Decane and 0.67 n-Heptane for cases 1, 2, and 3, respectively.

The case 1 problem configuration is from Abramzon and Sirignano [20], which provides details of the evaporation model implemented in PeleMP and a temperature-dependent liquid density is used in the PeleMP test. The results are shown in Fig. 5. The initial increase in diameter at the start of the test in the PeleMP values is due to a decrease in density as the droplet heats up. The reference results do not show this trend because a constant liquid density was used. Differences between the results are due to discrepancies in transport and thermodynamic properties. Overall, good agreement exists between the published numerical results and the PeleMP results, helping to verify the implementation of the evaporation model for a single-component liquid.

Case 2 results shown in Figs. 6 and 7 compare the multicomponent evaporation model implemented in PeleMP with the numerical results in [21]. Similar to case 1, temperature, droplet diameter, and n-Octane mass fractions are overpredicted, but overall agreement is good.

Case 3 compares PeleMP multicomponent evaporation model results with experimental values, and are shown in Fig. 8. PeleMP slightly overpredicts temperature and droplet size for all cases relative to the reference values; this is likely due to discrepancies in transport and thermodynamic properties for the numerical results. Overall, good agreement exists between the PeleMP results and the literature results, verifying the implementation of the spray evaporation model for single droplet cases.

4.2 Spray Injection. PeleMP coupled with PeleC is used to simulate the Spray A injection test case from the engine combustion network (ECN) [36]. The experiment involves injecting n-Dodecane into a gas consisting of mostly nitrogen at diesel-relevant conditions to test spray behavior in nonreacting conditions. The problem configuration is listed in Table 2. The domain is 6 cm in the jet streamwise direction and 1.2 cm in the other two directions. The base grid resolution is $375\,\mu$m, and three additional levels of refinement are added, resulting in a grid resolution of $46.875\,\mu$m at the finest level. The grid is refined based on temperature gradients of 10 K or greater, and refinement is fixed near the jet nozzle. No turbulence, turbulent dispersion, or droplet coalescence models are used in the numerical tests. The liquid properties were provided by NIST [37]. The KHRT model [24,38] implemented in PeleMP is used for this problem. For the breakup model, a constant liquid surface tension of $\sigma = 15$ dyne/cm is used, and the breakup
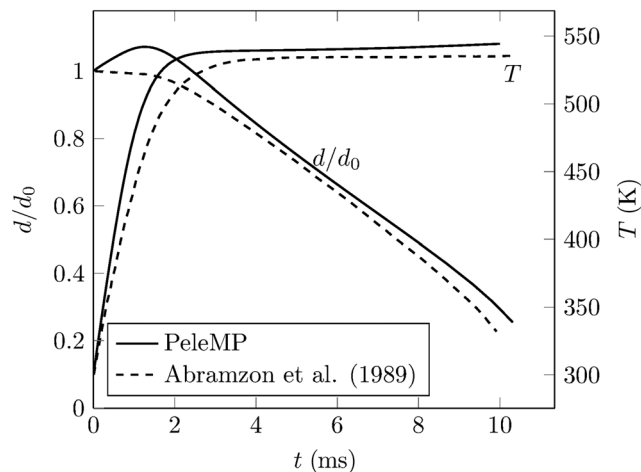

Fig. 5 Droplet normalized diameter and temperature for case 1 from Table 1
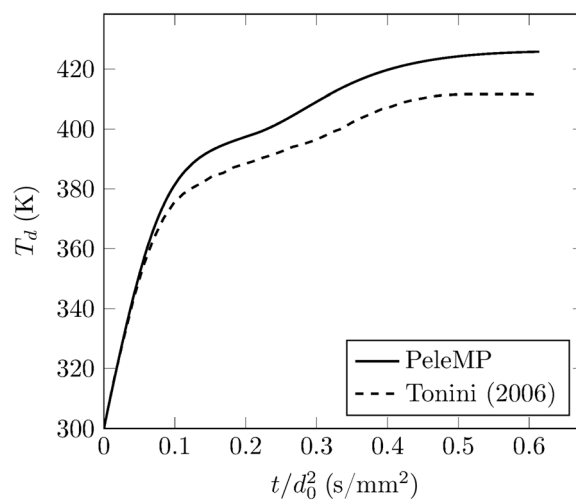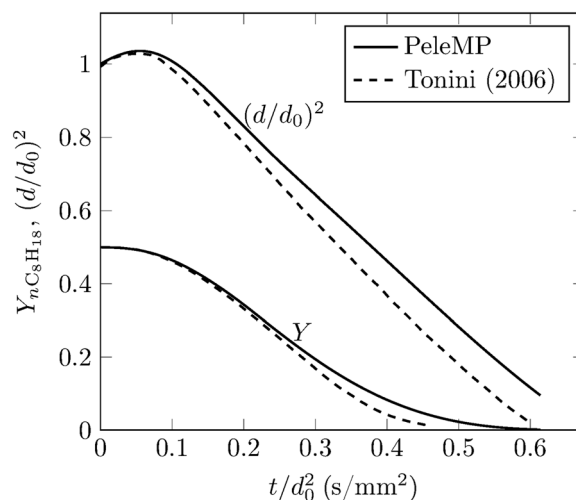

Fig. 6 Droplet temperature for case 2 from Table 1

Fig. 7 n-Octane liquid mass fraction and normalized diameter squared for case 2 from Table 1

Table 1 List of single droplet verification parameters

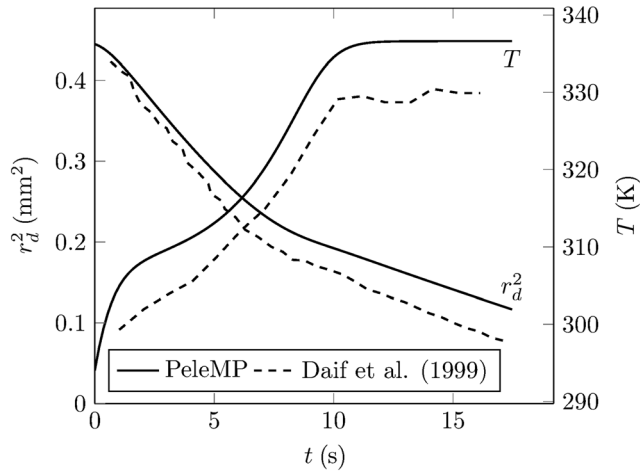| Case	d_0	T_d	u	T_g	p_g	Ref.
1	0.1 mm	300 K	15 m/s	1500 K	10 atm	[20]
2	2 mm	300 K	6.78 m/s	1000 K	1 atm	[21]
3	1.334 mm	294 K	3.1 m/s	348 K	1 atm	[35]

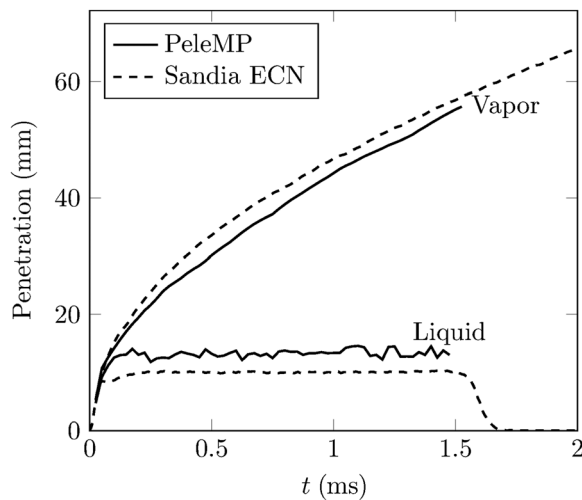**Fig. 8 Droplet radius squared and temperature for case 3 from Table 1**

Fig. 9 Liquid and vapor penetration with comparisons for Spray A case

parameters are $B_0 = 0.61$, $B_1 = 7.3$, and $C_3 = 5.3$. This test was performed on 20 Frontier nodes using approximately 60 node-hours. More configuration details regarding the injection routines are provided by Nguyen et al. [39], who performed a similar numerical test using commercial software.

Figure 9 shows the liquid and vapor penetrations compared to the experimental results from the ECN [36]. The vapor penetration is defined as the furthest downstream cell with a gas phase fuel mass fraction greater than 0.001 [40]. The liquid penetration is defined as the downstream location that contains 97% of the total liquid mass in the domain. The PeleMP results show an underprediction of the vapor penetration and an overprediction of the liquid penetration. These discrepancies are consistent with other numerical results using similar modeling and postprocessing methodologies. These results help verify the implementations for the spray injection routines, droplet-gas coupling for mass and momentum, and the KHRT breakup model.

4.3 Radiation Solver. The implementation of the P1 solver is verified through the MMS, which is a method to verify the implementation of the numerical solutions of PDEs [41]. The idea is to first construct a solution in the analytical form and then use the manufactured solution to derive the corresponding source term on the right-hand side of the governing equation. With this source term,

Table 2 Spray A problem configuration

p_g	T_g	T_d	Jet diameter	$d_{d,0}$	Inj. angle	Total inj. mass	Inj. time
60 bar	900 K	363 K	90 μm	89 μm	20 deg.	3.46 mg	1.54 ms

a numerical solution is calculated, which can be compared to the prescribed analytical solution. When constructing manufactured solutions, it is necessary to keep the solution differentiable, so that all the derivatives in the governing equation can be verified. In the meantime, the manufactured solution does not need to be physical.

The example unit MMS test for the P1 RTE solver is with constant and uniform absorption coefficients $\beta = \kappa = 1.0$. The P1 governing equation, Eq. (26), is now given as

$$\frac{1}{3}\nabla \cdot (\nabla G) - G = S_{\text{MS}} \tag{33}$$

where the source S_{MS} is derived from the manufactured solution G_{MS}. We choose to use an analytical combination of trigonometric functions for G_{MS}. The manufactured solution is prescribed as

$$G_{\text{MS}} = \sin\frac{n\pi x}{L}\cos\frac{n\pi y}{L}\sin\frac{n\pi z}{L} \tag{34}$$

Substituting the prescribed solution into the governing equation, Eq. (33), we get the analytical form of the source term

$$S_{\text{MS}} = -\left(1 + \frac{n^2\pi^2}{L^2}\right)G_{\text{GS}} \tag{35}$$

The verification of the boundary conditions follows a similar procedure. The Robin-type boundary condition for the P1 model under MMS is

$$-\frac{2}{3}\widehat{\mathbf{n}} \cdot \nabla G_w + G_w = S_{\text{MS},w} \tag{36}$$

For example, $S_{\text{MS},w}$ at the walls in the x direction is

$$S_{\text{MS},w} = \left(\pm\frac{2}{3}\frac{n\pi}{L}\cos\frac{n\pi x}{L} + \sin\frac{n\pi x}{L}\right)\cos\frac{n\pi y}{L}\sin\frac{n\pi z}{L} \tag{37}$$

The L_1 norm of the error between the computed and prescribed G is used to show the order of convergence,

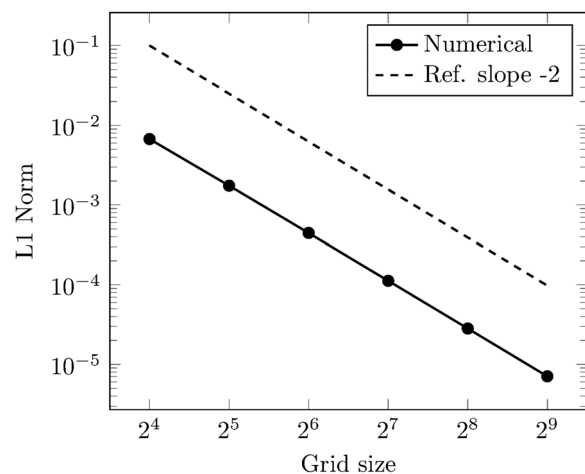$$L_1 = \frac{1}{N}\sum_{i}^{N}|G - G_{\text{MS}}| \tag{38}$$

Fig. 10 L_1 norm of error between computed and prescribed solution for the MMS problem

The results with $n = 3$ in a cubic domain are shown in Fig. 10. The order of accuracy is found to be second-order for the errors with increasing grid size. Utilizing this method of MMS verification has been integral to the code development process, serving as continuous integration (CI) unit tests to identify any unintended changes that could potentially lead to test failures.

4.4 One-Dimensional Laminar Flame. The coupled soot, radiation, and gas-phase models are verified with a one-dimensional laminar burner-stabilized premixed flame configuration. The lower and upper x-direction boundary conditions are inflow and outflow, respectively. Although the physics of the problem are one-dimensional, the numerical results are computed in Pele in both 2D and 3D, with periodic boundary conditions for the remaining dimensions. Table 3 shows parameters used for this test case. To reduce computational time, Cantera [42] is used to compute the steady-state solution for the gas phase without soot, and this steady-state solution is imported into PeleC or PeleLMeX as the initial condition for the gas phase. The case is run until the solution reaches a pseudo-steady-state, which occurs at a solution time of 0.022 s.

The solution profiles from Pele are compared with results from FlameMaster [43] that contains the same HMOM soot model but with radiation disabled (since it is modeled differently from Pele). A reduced chemical mechanism of 47 species and 224 reactions from Bisetti et al. [44] is used to model the gas-phase chemistry; this mechanism includes PAH chemistry up to naphthalene ($C_{10}H_8$), which is the lone soot inception species.

Figure 11 shows the temperature and soot volume fraction profiles for the laminar premixed flame case. Good agreement is seen between the FlameMaster and Pele solution without radiation. Very minor differences in the temperature and soot volume fraction are due to differences in inflow and outflow boundary conditions and transport property values between the codes.

Figures 12 and 13 also show good agreement between the FlameMaster and Pele results for the soot number density and naphthalene mass fractions. Compared to FlameMaster, Pele slightly overpredicts the peak number density but underpredicts the downstream number density. These trends in the number density are consistent with the differences in the naphthalene mass fraction, which is most sensitive to the minor code differences.

Radiation effects are studied next by coupling the P1-Gray radiation model to the soot and flow solvers. In Fig. 11, the temperature decreases in the postflame region (consistent with the experimental measurements discussed below). The lower temperature results in a lower naphthalene mass fraction, decreasing the rate of soot inception so a lower soot number density and lower soot volume fraction. The response of soot yield to temperature is
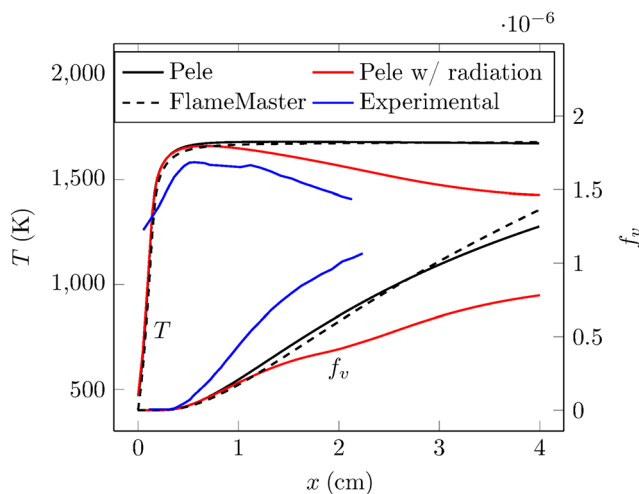
Table 3 Thermodynamic conditions, inflow conditions, and domain length for the one-dimensional laminar premixed flame

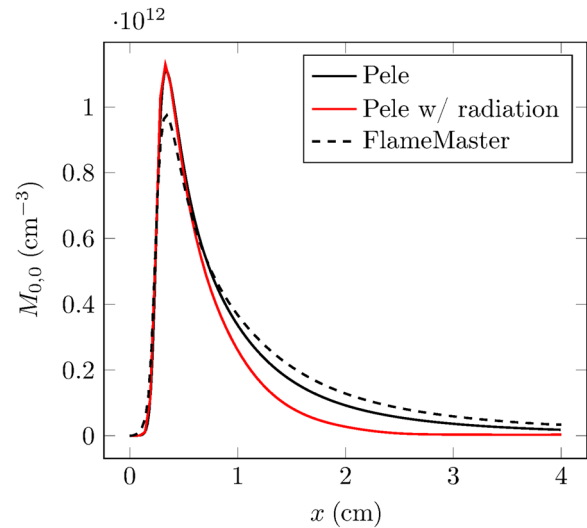| Fuel	ϕ	P_g (bar)	T_{inlet} (K)	$\dot{m}$ (kg m^{-2}s^{-1})	L (cm)
C_2H_4	2.64	1	400	0.0793	4

Fig. 12 Laminar premixed flame soot number density profile

complex: soot tends to increase with increasing temperature at low temperatures and decreases with increasing temperature at high temperatures, the so-call bell-shaped behavior (see, e.g., the work of Blanquart and Pitsch [45] for further details).

Finally, the configuration of the test case corresponds to the burner-stabilized flame experiments performed by Xu et al. [46] and Menon et al. [47]. Included in Fig. 11 are profiles from the experiments of Menon et al. [47]. Heat loss to the burner in the experiment is not modeled in our numerical results, leading to the increased temperature relative to the experiment. For this reason, when comparing simulations to experimental measurements in this burner-stabilized flame configuration, the experimental temperature profile is typically enforced in the simulations. However, such an
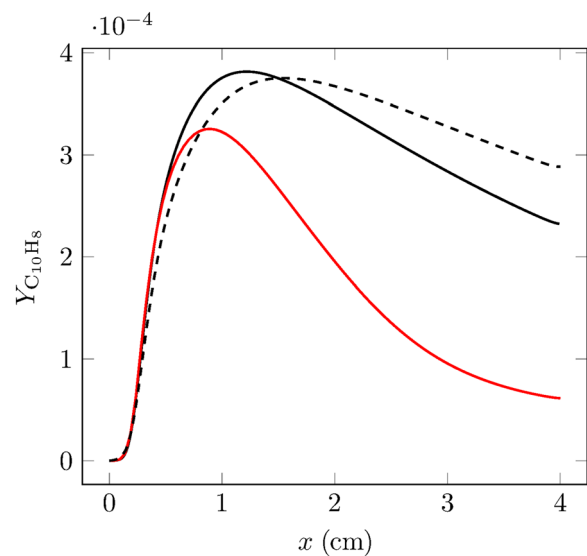

Fig. 11 Laminar premixed flame temperature profile

Fig. 13 Laminar premixed flame naphthalene (soot precursor) mass fraction profile

Table 4 Heterogeneous HPC configurations

Machine	Cores per node	GPUs/GCDs[1] per node	GPU spec.	Number of nodes
Frontier	64	8	AMD MI250X	9408
Crusher	64	8	AMD MI250X	192
Perlmutter	64	4	NVIDIA A100	1536
Summit	42	6	NVIDIA Tesla V100	4600
Cori Haswell	32	N/A	N/A	2388

[1]GCD: Graphics Compute Dies

enforcement was not pursued here since the main objective was to compare FlameMaster with Pele to verify the HMOM soot model implementation: the experimental measurements are only shown here as a "sanity check" on the numerical results. Nonetheless, the qualitative decrease of temperature in the postflame region is consistent with the Pele results when radiation is considered. Interestingly, the soot volume fraction is underpredicted compared to the experimental measurements even though the temperature is overpredicted, which is the opposite behavior of soot with temperature when radiation is enabled in Pele. This suggests that the simulation temperature is in the high-temperature region of the soot bell-shaped behavior, while the experimental temperature is in the low-temperature region of the soot bell-shaped behavior.

5 Algorithm Performance

In this section, we report the performance benchmarks for both on-node and distributed memory cases. The on-node benchmarks show the speedups from the GPU accelerators. Performance metrics are determined on Summit, Crusher, and Frontier at the OLCF, as well as Cori and Perlmutter at NERSC. Information about the hardware is provided in Table 4. The software environments for the OLCF machines are shown in Table 5

5.1 Distributed Particle Tests. To test the scaling performance of the spray models in PeleMP, distributed particle tests are performed. For these tests, spray droplets are initialized uniformly throughout a 3D, fully periodic domain and given an initial velocity in a single direction to test data communication as the particles change location in memory. It is important to note that these tests are designed to represent the "worst case scenario" for a spray modeling problem. In most practical spray problems, droplets will be concentrated in specific regions, typically near or on the finest level, which will reduce the amount of communication done for particle redistributions. Additionally, adding reaction solutions to the simulation will increase the algorithmic intensity, thus diminishing the impact of particle communication and creation on performance.

Figure 14 shows the speedup when switching from a CPU-only cluster to a CPU/GPU machine for PeleC/PeleMP. Distributed particle tests are performed on 8 nodes on Cori Haswell (for CPU performance metrics) and Summit (for GPU performance metrics) for an increasing number of particles. This particular test has a base mesh of 256^3 cells with 2 additionally refined levels in the center of the domain with 128^3 cells on each level. From the figure, there is a speedup of almost 100 times when no particles are in the domain. As particles are added to the domain, more time is spent in particle communication and the GPU-based performance gains decrease.

**Table 5 Software environment for the performance benchmarks**

Frontier and Crusher		Summit	
Software	Version	Software	Version
Clang	15.0.0	GCC	8.3.1
MPICH	8.1.23	Spectrum MPI	10.4.0.3
ROCm	5.2.0	CUDA	11.0.3
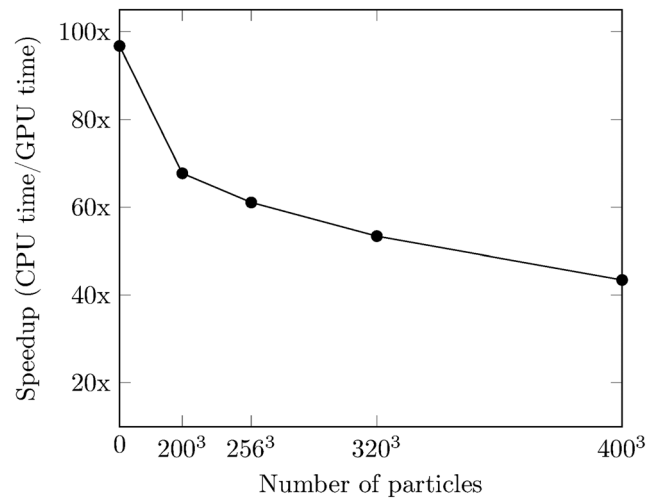
Fig. 14 Distributed particle performance comparison between 8 Cori Haswell nodes (CPU only) and 8 Summit nodes (CPU/GPU) for increasing particle counts

However, even with 64×10^6 particles in the domain the code achieves a 43 times speedup.

Figure 15 shows distributed particle performance for PeleC/PeleMP and PeleLMeX/PeleMP on Crusher. The test has 128^3 cells and 160^3 particles per node. As the node count increases, parallel efficiency begins to decrease for both codes. The drop in parallel efficiency at the highest node count for the PeleLMeX/PeleMP solution is due to the projection routines in PeleLMeX, which require more communication and can be difficult to parallelize.

Figure 16 shows the weak scaling performance of a PeleC/PeleMP distributed particle test on Frontier. Two tests are performed; one with a single refined mesh and one with no refinement. For each node, there are 128^3 cells on the base mesh with
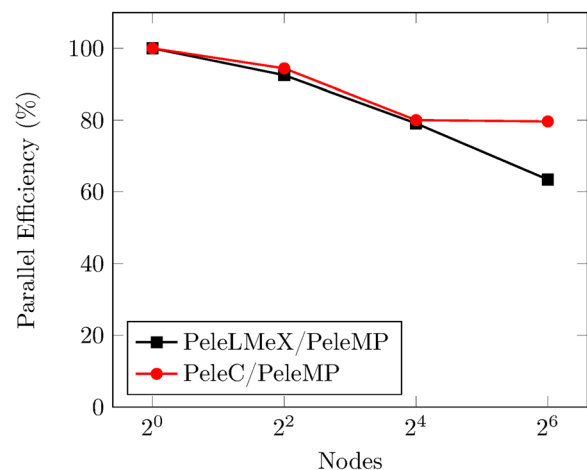
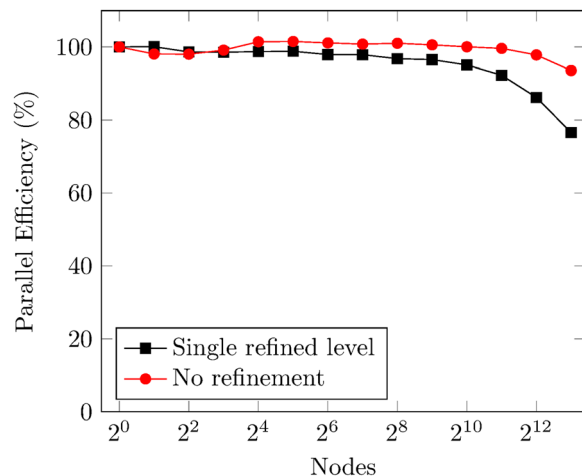**Fig. 15 Distributed particle weak scaling performed on Crusher**

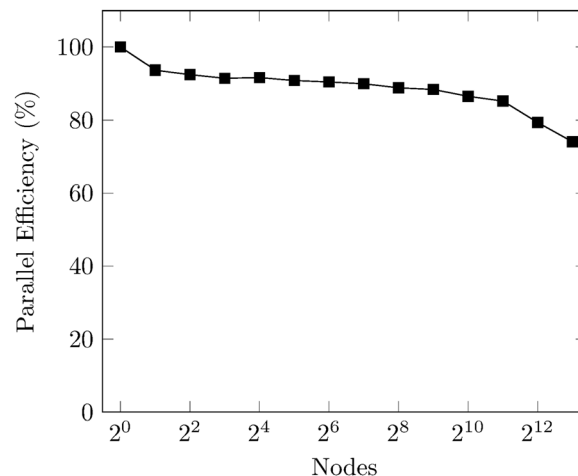**Fig. 16 PeleC/PeleMP distributed particle weak scaling performed on Frontier**

Fig. 17 Weak scaling of PeleLMeX/PeleMP simulating the burner case with 819,200 cells/GPU on Frontier up to 65,536 MPI ranks (one MPI rank per GPU)

128^3 refined cells (if multiple levels are used) and 256^3 particles. Each test is run for 20 coarse time steps. The tests are run up to 8,192 nodes, which is 87% of Frontier. The first time-step and initialization routines are not included in the timings because they would become negligible for longer runs. At higher node counts, the performance of both tests degrades; this is largely due to the increased cost associated with particle redistribution routines. Particle redistribution requires device to host and internodal communication, making it difficult to parallelize. However, the performance degradation is worse for the refined level test. A significant contribution to the refine level performance degradation is the Ghost and Virtual particles setup routines. The flat mesh test (no refinement) does not use Ghost or Virtual particles. Since AMReX particle creation is performed on the host and communicated to the device, Ghost and Virtual particle setup routines do not take full advantage of the device speedup. For the current test case, the Ghost/Virtual particle creation routines represent approximately 20% of the run time for all node counts. By comparison, the time spent setting up Ghost and Virtual particles for the Spray A simulation described in Sec. 4.2 is around 6%.

5.2 Soot and Radiation Tests. In this section, both the on-node and internode performances are benchmarked. A synthetic flame profile is employed as the on-node benchmark, showcasing the acceleration achieved with a single GPU. A single-step calculation based on one snapshot of a flow field on a three-dimensional cuboid mesh is used to isolate the evaluation of radiative transfer from the changing flow fields. The domain size is $12.5\,cm \times 12.5\,cm \times 75\,cm$. The side boundaries (in the x and y directions) are treated as cold and black walls. The top and bottom boundaries (in the z direction) are treated as reflective walls, where the Neumann boundary condition is applied. Values for T, P, Y_k, and f_v are fabricated at realistic scales encountered in flame simulations. The mesh resolutions for three different simulations are listed in Table 6.

The performance of the radiation solver is benchmarked on both Summit and Crusher, as shown in Table 6. The current performance benchmarks are for single-level AMR and will serve as the baseline for more complicated scaling tests. The MG solver stops iterating when the relative residuals are less than 10^{-6}. Different levels of MG
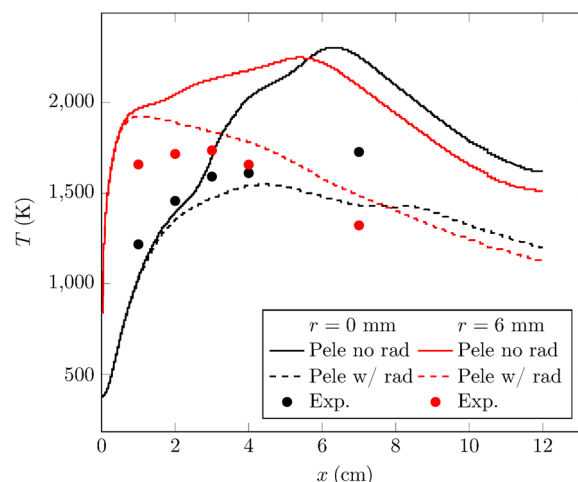
Fig. 18 Coflow temperature in axial direction with experimental results from D'Anna et al. [48]

are applied, and the optimal number of MG levels is found to be around 4 or 5. As expected, the results show that the speedup by the GPUs depends on the size of the mesh.

To show the scalability, we examine the weak scaling of the burner configuration with PeleLMeX described in Sec. 4.4. The two periodic dimensions are scaled up with the MPI ranks while keeping the number of cells per GPU constant. Each GPU operates on approximately 819,200 cells. The weak scaling employs up to 65,536 GPUs evenly distributed among 8,192 nodes on Frontier, which is 87% of the total number of nodes available (9408 nodes). A total number of 53.7 billion cells are used in the largest case. Radiation and soot are reported to take less than 8% of the time throughout the scaling test. The weak-scaling performance on Frontier is shown in Fig. 17. Two major drops in parallel efficiency are observed. The initial performance drop of approximately 6.3%

Table 6 On-Node performance of the P1 radiation solver on Summit and Crusher(s)

Mesh	IBM POWER9	Nvidia V100	AMD EPYC 7A53	AMD MI250X
$32 \times 32 \times 192$	0.23	0.09	0.16	0.05
$64 \times 64 \times 384$	4.26	0.32	2.19	0.24
$128 \times 128 \times 768$	32.2	0.94	19.5	0.86

occurs between the single and double node tests. The slope of the performance drop remains steady until it increases at 4,096 nodes. For the largest case (with 65,536 MPI ranks), the parallel efficiency decreases by approximately 26% from the single node performance.

6 Results

In this section, three demonstration simulations are presented that incorporate the PeleMP multiphysics models in PeleLMeX. Specifically, a simulation is performed of a sooting ethylene-air laminar coflow flame and another of a turbulent ethylene jet flame on Frontier. These simulations aim to investigate the intricate interactions between flow, soot, and radiation. Additionally, simulations of bluff-body swirl-stabilized spray flames with SAFs are performed on Perlmutter. These simulations study how different ignition properties of the fuels impact the flame stabilization. Future simulations of high-speed propulsion will utilize PeleC coupled with PeleMP for modeling compressible flows.

6.1 Sooting Laminar Nonpremixed Coflow Flame. An axisymmetric, laminar, nonpremixed coflow flame of ethylene-air is one of the target flames for the International Sooting Flames (ISF) Workshop for the Measurement and Computation of Reacting Flows with Carbon Nanoparticles. The configuration comes from experiments performed by D'Anna et al. [48] and consists of two concentric tubes below a burner-attached flame; the inner tube is a 12 mm diameter tube issuing fuel and the outer tube is a 55 mm diameter tube issuing air. The fuel passage has a flowrate of $3.85\,\text{cm}^3/\text{s}$ with a flow velocity of 3.40 cm/s. The air passage has a flowrate of $700\,\text{cm}^3/\text{s}$ with a velocity of 30.9 cm/s.

In the numerical configuration, the tubes are modeled as inlets at the lower jet normal domain boundary. The air enters at 300 K, and the fuel enters at 375 K to mimic heat transfer to the burner from the flame, which is not modeled. Different inlet fuel temperatures were tested with negligible impact on downstream temperature and soot volume fraction (only a very minor shortening of the flame and corresponding increase in peak temperature and peak soot volume fraction as the fuel temperature was increased). The computational domain is 12 cm in the jet streamwise direction (z direction) and 6 cm in the other directions (x and y directions). Since the flame is laminar and radially symmetric, only a quarter of the domain is modeled to reduce the computational cost. This is achieved by using symmetry boundary conditions at the lower x and y boundaries and outflow boundary conditions at the upper z boundary. The base mesh is $64 \times 64 \times 128$ cells in the $x, y,$ and z directions, respectively. There are two additional levels of refinement with refinement ratios of two, meaning the grid resolution on the finest level is 234 μm. This simulation uses the same 47 species and 224 reactions from Bisetti et al. [44] described in Sec. 4.4.

The centerline temperature values, shown in Fig. 18, show good agreement with the experimental measurements when radiation effects are modeled (the dashed lines). Compared to the experimental measurements, the soot volume fraction along the centerline (Fig. 19) is underpredicted by a factor of a few, which is not atypical for soot predictions. In fact, the present predictions along the centerline are comparable to previous simulations of the same flame with different soot models and chemical mechanisms (see, e.g., [49]). For the models considered in the present work, the use of a reduced chemical mechanism with naphthalene as the sole PAH and the use of only first-order moments could contribute to the minor underprediction. However, the overall qualitative structure of the soot predictions, including the locations along the centerline where the soot volume fraction begins to gradually increase and then sharply decrease, is consistent with the experimental measurements.

6.2 Turbulent Sooting Flame. Soot and radiation models have been employed in a simulation of a laboratory turbulent sooting ethylene jet flame [50] using PeleLMeX. This flame features a central ethylene fuel jet with a diameter of 3.2 mm and a velocity of 54.7 m/s, resulting in a Reynolds number of 20,000. The flame is

stabilized by a pilot of ethylene/air at an equivalence ratio of 0.9 surrounding the fuel nozzle. The simulation features a base grid of $128 \times 128 \times 256$ cells with a cell size of 1 mm. This simulation uses the same 47 species and 224 reactions from Bisetti et al. [44] described in Secs. 4.4 and 6.1. Figure 20 shows the instantaneous temperature, soot volume fraction, and radiative emission in the turbulent flame simulation. As can be seen, the structure of this flame features a significant amount of wrinkling, with soot predominantly being produced in the vicinity of high-temperature wrinkled flame regions further downstream that coincide with high radiative emission. While there is an interaction between the fast fuel jet and the pilot at the base of the flame, a fully turbulent flame only develops beyond approximately 10 mm. Similarly, there are small amounts of soot formed upstream, however, regions with significant amounts of soot are only formed further downstream. These regions mostly feature flame curvature with the center of curvature residing in the fuel stream. It has been shown previously that the formation of soot in a turbulent flame is significantly affected by turbulent mixing effects and a disparity between fluid and soot transport mechanisms [51,52]. Similar to previous work, large amounts of soot are formed close to the flame and spread toward richer regions due to turbulent mixing [52].

This simulation demonstrates the feasibility of Pele to simulate soot formation coupled with thermal radiation from the soot particles in a complex turbulent flow environment. The peak temperature drops around 25 K due to the cooling from radiation. Although temperature differences due to radiative transfer are not large, the peak soot volume fraction almost drops by half, from 2.54 ppm to 1.44 ppm. The strong soot growth sensitivity to temperature emphasizes the importance of including radiation [53]. The coupling between chemistry, flow, soot, and radiation is intertwined, especially considering the bell-shaped behavior [45] for soot and temperature. The presence of soot significantly enhances the radiative emission from the flame. For the size of this flame, only a relatively small portion of the radiative heat is reabsorbed. The high-temperature regions of the flame are cooled down by the radiation and would affect soot generation. The resulting lower or higher soot (depending on which side of the bell curve) would, in turn, change the radiation patterns. Further analysis of the simulation results will provide detailed insight into the soot formation processes in a turbulent flame including the relationship of soot inception, growth, and oxidation as a function of particle residence times determined by turbulent mixing under the influence of radiation in the jet flame.
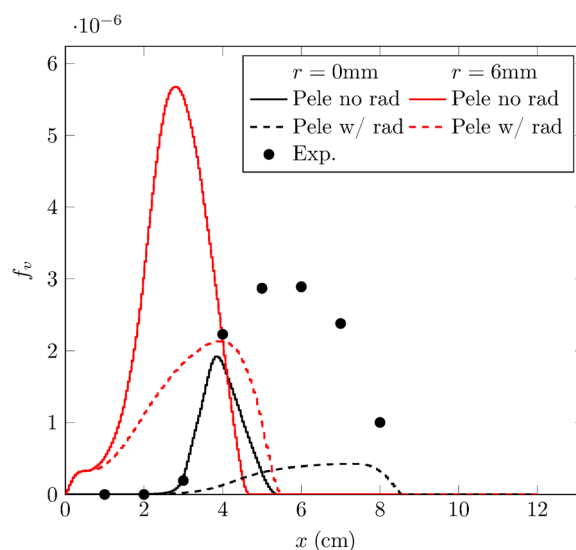

Fig. 19 Coflow soot volume fraction in axial direction with experimental results from D'Anna et al. [48]
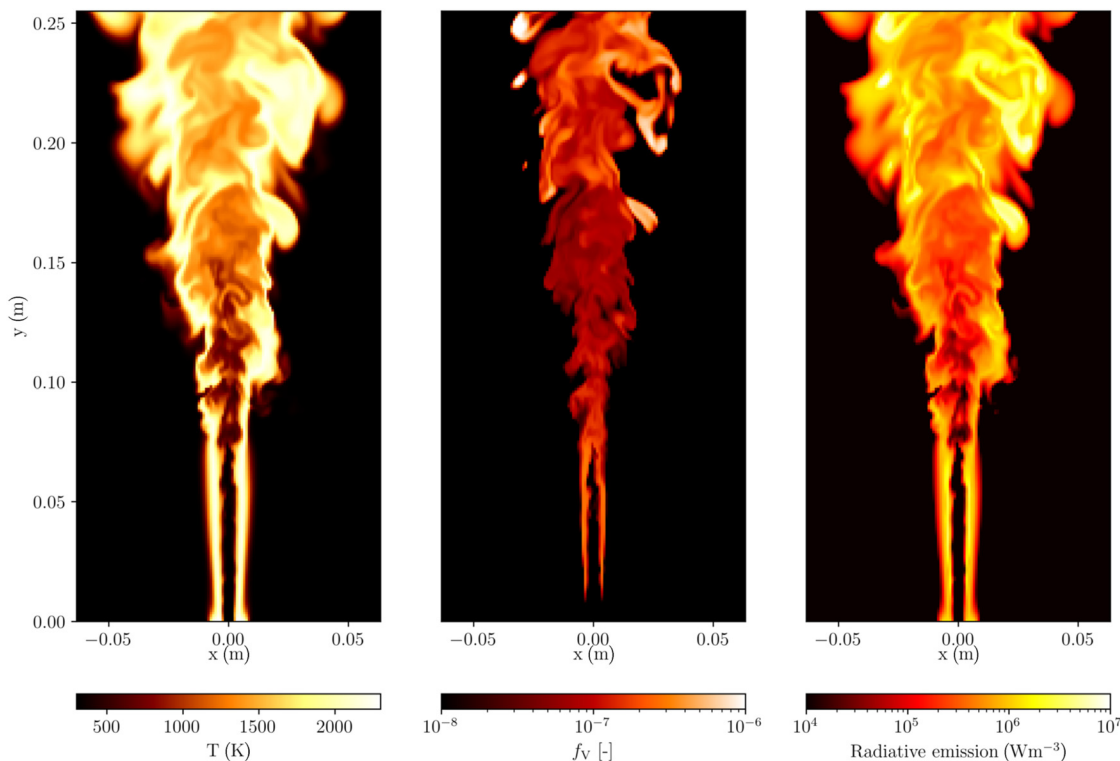
Fig. 20 Temperature, soot volume fraction, and radiative emission in the turbulent sooting flame

To further test the robustness of Pele for large-scale turbulent simulations, we refine the bottom-level Cartesian mesh to $256 \times 256 \times 512$ and perform simulation with three levels of AMR on 8,192 nodes (with 65,536 GPUs) on Frontier. The base level contains 33.6×10^6 cells, with a resolution on the finest level of $62.5\ \mu m$. This resolution is close to the necessary DNS resolution (O (10) μm). Achieving this resolution requires exascale computing resources. With the realistic physics included in the flame simulation, this run has demonstrated the capability and robustness of PeleMP to utilize almost all of Frontier for large-scale high-fidelity simulations, leaving additional room to expand the computational domain, to refine the mesh, and to include more sophisticated multiphysics models.

6.3 Bluff-Body Swirl Stabilized Spray Flame. SAFs are of particular interest to reduce emissions and develop renewable energy sources for the aviation sector. The National Jet Fuel Program (NJFP) tested several alternative nonfossil fuels that can be used to mitigate climate change and air quality [54]. Predictive and efficient computational models are required to reduce costs related to testing SAFs and design more efficient aviation engines. The PeleMP spray model coupled with PeleLMeX on exascale supercomputers enabled a DNS investigation of a laboratory-scale combustor. The simulation is designed to provide a greater understanding of flame stabilization dynamics and evaluate the efficacy of turbulent combustion models. Two different simulations are performed: one with the reference Jet-A fuel and another with the SAF Alcohol-To-Jet C1 fuel. The numerical simulation is based on the atmospheric pressure Rich-Quench-Lean (RQL) burner experiment developed by the University of Cambridge [55]. The flow recirculation zones are captured in the simulation by including the bluff-body geometry using the EB approach and placing the liquid fuel injector at the same physical location as in the experiment. The simulations used a base grid with $128 \times 128 \times 256$ cells with three levels of refinement yielding a resolution of $78\ \mu m$. The dynamic adaptive mesh refinement resulted in a total of approximately 350×10^6 cells. The simulations used the reduced UIUC mechanisms for Jet-A and C1 with, respectively, 48 and 57 species [56,57].

The C1 fuel is comprised primarily of C12 and C16 isoparaffins [58], so liquid C1 is modeled as a two-component surrogate comprised of 0.135 isocetane and 0.865 isododecane by volume. The reduced chemical mechanism models the fuel as a single-component surrogate, so the PeleMP implementation allows for each liquid component to be evaporated onto the single-component fuel species in the gas phase. Liquid Jet-A is modeled as a single component surrogate. The spray injection is modeled in accordance with the experiment as a hollow cone with a 60 deg angle [59,60]. A spread angle of 5 degrees is included to reproduce the stochastic variation in the cone angle. The boundary condition for the liquid uses the dilute spray assumption where droplet size is specified with a Sauter Mean Diameter of $60\ \mu m$ and a Weibull distribution with the exponential factor equal to 4. The simulations used 256 GPU nodes on NERSC Perlmutter, requiring approximately 35,000 node hours each.

Figure 21 presents the instantaneous distribution of heat release rate and stream-wise velocity for a cross-sectional plane and the liquid fuel injection downstream of the bluff body. The figure shows
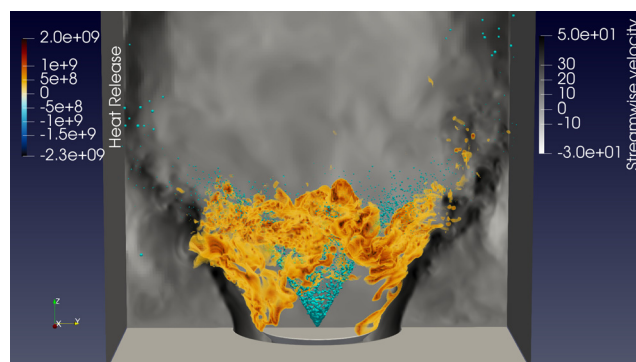

Fig. 21 Instantaneous volume rendering of the heat release rate showing the combustion process for Jet-A. The stream-wise velocity is presented for a cross-sectional plane and the liquid phase is represented by the isosurface in green.
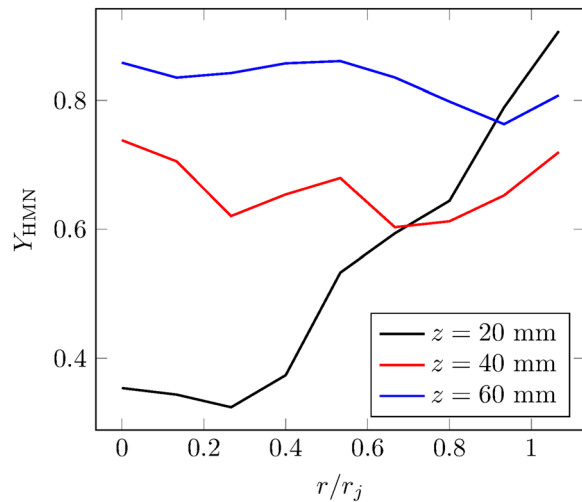
Fig. 22 Mean droplet liquid isocetane mass fraction conditioned on the radial direction for different streamwise locations

the complexity of the flame stabilization for this configuration. The liquid spray interacts with the heat release rate layer and quickly evaporates. The interaction between the incoming turbulent flow and the fuel mixing causes local flame extinction to occur in the shear layer region. The hot air in the recirculation zone provides enthalpy and chemical radicals required to reconnect the flame in the extinguished regions.

Figure 22 presents the mean droplet isocetane (HMN) mass fraction conditioned on the radial direction for different locations in the streamwise direction. The statistics presented here were obtained by binning all the Lagrangian particles into a radial grid ranging from 0 to 60 mm in length with a spatial resolution of 3 mm. The isocetane mass fraction boundary condition is 0.135. However, as the droplets are advected downstream and start to lose mass, preferential evaporation effects show a larger evaporation of isododecane, resulting in the greater isocetane mass fraction. The results are consistent with the multicomponent single droplet simulations presented by Bonanni and Ihme [61] where heavier and less volatile components take longer to evaporate. The fuel components present different chemical characteristics, e.g., ignition delay time, that can affect the flame stabilization dynamics. Despite the simplified representation of the fuel by the chemical mechanism, the Lagrangian multicomponent spray model implemented in PeleMP enabled the identification of preferential evaporation effects in aero-engine configurations.

7 Summary and Scientific Outlook

PeleMP expands the Pele reacting flow solver code suite to include multiphysics modeling. The mathematical and algorithmic aspects of the spray, soot, and radiation models have been presented here, including their coupling with the time advancement of each of the gas phase solvers. The implementations are verified by comparing results to existing numerical and experimental literature. Benchmark tests are presented that demonstrate the weak scaling behavior of both PeleC and PeleLMeX on multiple supercomputers, including Frontier, the latest exascale supercomputer at the OLCF. Finally, results from three different production simulations performed on heterogeneous supercomputers are presented: a laminar nonpremixed sooting coflow ethylene-air flame; a turbulent sooting nonpremixed ethylene-air piloted jet flame; and a turbulent bluff-body swirl stabilized jet-fuel spray flame. The two sooting flames demonstrate the predictive capabilities of the soot and radiation models provided by PeleMP when coupled with the low-Mach flow solver PeleLMeX. The swirl stabilized spray flame demonstrates the Lagrangian spray model in PeleMP coupled with PeleLMeX and its interaction with a reacting gas phase and wall-bounded domain, represented by EB.

The swirl stabilized spray flame simulation will be expanded in future work to fully leverage PeleMP's exascale capabilities. For example, simulating the swirl stabilized spray flame closer to realistic operating conditions ($T \approx 453$ K and $p \approx 3$ bar) would require twenty times the number of cells, or approximately 7 billion cells; a simulation of this magnitude would necessitate exascale computing resources.

In the near future, zero carbon fuels will replace hydrocarbon fuels in hard-to-electrify sectors, such as marine shipping, gas turbines for dispatchable power generation, and agricultural and mining equipment. A better understanding of the physical and chemical properties of the different fuels as they affect vaporization, lean blowout, and ignition will be required to develop and optimize these technologies. High-fidelity DNS and LES in laboratory-scale configurations at relevant device thermochemical conditions will play an important role alongside experimentation. As an example, simulations can be used to understand multi-injection ignition strategies for difficult-to-ignite alternative liquid fuels like ammonia that are piloted with diesel fuels. While the dilute multicomponent spray capabilities in PeleMP provide the capability to probe preferential vaporization, mixing, and ignition, further improvements in spray submodels are needed. For example, fuel wall film and splash models will provide detailed characterization of vaporization and mixture formation in near-wall regions, especially as spray, mixing, and reaction co-exist in compact gas turbine engine configurations.

The capability of capturing soot, radiation, and spray in reactive flow simulations using complex geometries and relevant engine conditions marks a new era in the development of modern aero-engines. However, further improvements in the soot capabilities are required. The increase in cloudiness related to contrail formation results in the largest contribution of the aviation sector to global warming [62]. The production of contrails and their effects on global warming are intimately related to the fuel chemistry and soot emitted by the engine [63]. Accurate predictions of particle size distribution have an impact on the correct estimate of contrail ice formation [64]. The current HMOM soot model implementation in PeleMP accounts for the mean primary particle diameter; however, future efforts will include capabilities for evolving the full soot size distribution. The radiation model will be extended to include nongray effects through the full spectrum k-distribution model and higher-order RTE solvers. Finally, increasingly complex transportation fuel mixtures arise in the development of sustainable sources. A generalized approach is under development for PeleMP's liquid fuels capability that allows the evaluation of thermodynamic and transport properties of practical fuels based only on the intrinsic functioCnal groups and their relative abundance [65]. This capability will open the pathway to automated coupling to novel fuel development and exploration. In all, the current and future multiphysics capabilities in PeleMP coupled with the compressible and low Mach solvers in the Pele suite have the potential to be an indispensable tool set to support critical technology advances that address the nation's evolving energy and climate change mitigation needs.

Data Availability Statement

The datasets generated and supporting the findings of this article are obtainable from the corresponding author upon reasonable request.

References

[1] Chen, J. H., Choudhary, A., de Supinski, B., DeVries, M., Hawkes, E. R., Klasky, S., Liao, W. K., Ma, K. L., Mellor-Crummey, J., Podhorszki, N., Sankaran, R., Shende, S., and Yoo, C. S., 2009, "Terascale Direct Numerical Simulations of Turbulent Combustion Using S3D," Comput. Sci. Discovery, **2**(1), p. 015001.

[2] Rieth, M., Gruber, A., and Chen, J. H., 2023, "A Direct Numerical Simulation Study on NO and N2O Formation in Turbulent Premixed Ammonia/Hydrogen/Nitrogen-Air Flames," Proc. Combust. Inst., **39**(2), pp. 2279–2288.

[3] Henry de Frahan, M. T., Rood, J. S., Day, M. S., Sitaraman, H., Yellapantula, S., Perry, B. A., Grout, R. W., Almgren, A., Zhang, W., Bell, J. B., and Chen, J. H., 2022, "PeleC: An Adaptive Mesh Refinement Solver for Compressible Reacting Flows," Int. J. High Perform. Comput. Appl., **2022**, epub.

[4] Day, M., Esclapez, L., Wimer, N., Bell, J., and Nonaka, A., 2022, "PeleLMeX," Computer Software.

[5] Pele Team, 2022, "PelePhysics, a Repository of Physics Databases and Implementation Code for Use With the Pele Suite,".

[6] Zhang, W., Almgren, A., Beckner, V., Bell, J., Blaschke, J., Chan, C., Day, M., Friesen, B., Gott, K., Graves, D., Katz, M., Myers, A., Nguyen, T., Nonaka, A., Rosso, M., Williams, S., and Zingale, M., 2019, "AMReX: A Framework for Block-Structured Adaptive Mesh Refinement," J. Open Source Softw., **4**(37), pp. 1–4.

[7] Hindmarsh, A. C., Brown, P. N., Grant, K. E., Lee, S. L., Serban, R., Shumaker, D. E., and Woodward, C. S., 2005, "SUNDIALS: Suite of Nonlinear and Differential/Algebraic Equation Solvers," ACM Trans. Math. Softw., **31**(3), pp. 363–396.

[8] Amsden, D. C., and Amsden, A. A., 1993, "The KIVA Story: A Paradigm of Technology Transfer," IEEE Trans. Prof. Commun., **36**(4), pp. 190–195.

[9] Subramaniam, S., 2013, "Lagrangian–Eulerian Methods for Multiphase Flows," Prog. Energy Combust. Sci., **39**(2–3), pp. 215–245.

[10] Mueller, M. E., Blanquart, G., and Pitsch, H., 2009, "Hybrid Method of Moments for Modeling Soot Formation and Growth," Combust. Flame, **156**(6), pp. 1143–1155.

[11] Ge, W., David, C., Modest, M. F., Sankaran, R., and Roy, S. P., 2023, "Comparison of Spherical Harmonics Method and Discrete Ordinates Method for Radiative Transfer in a Turbulent Jet Flame," J. Quant. Spectrosc. Radiat. Transfer, **296**, p. 108459.

[12] Lucchini, T., D'Errico, G., and Ettorre, D., 2011, "Numerical Investigation of the Spray–Mesh–Turbulence Interactions for High-Pressure, Evaporating Sprays at Engine Conditions," Int. J. Heat Fluid Flow, **32**(1), pp. 285–297.

[13] Marchioli, C., 2017, "Large-Eddy Simulation of Turbulent Dispersed Flows: A Review of Modelling Approaches," Acta Mech., **228**(3), pp. 741–771.

[14] Goryntsev, D., Sadiki, A., Klein, M., and Janicka, J., 2010, "Analysis of Cyclic Variations of Liquid Fuel–Air Mixing Processes in a Realistic DISI IC-Engine Using Large Eddy Simulation," Int. J. Heat Fluid Flow, **31**(5), pp. 845–849.

[15] Robert, A., Zaccardi, J.-M., Dul, C., Guerouani, A., and Rudloff, J., 2019, "Numerical Study of Auto-Ignition Propagation Modes in Toluene Reference Fuel–Air Mixtures: Toward a Better Understanding of Abnormal Combustion in Spark-Ignition Engines," Int. J. Engine Res., **20**(7), pp. 734–745.

[16] Esclapez, L., Ma, P. C., Mayhew, E., Xu, R., Stouffer, S., Lee, T., Wang, H., and Ihme, M., 2017, "Fuel Effects on Lean Blow-Out in a Realistic Gas Turbine Combustor," Combust. Flame, **181**, pp. 82–99.

[17] Gorokhovski, M., and Herrmann, M., 2008, "Modeling Primary Atomization," Annu. Rev. Fluid Mech., **40**(1), pp. 343–366.

[18] Arienti, M., Pan, W., Li, X., and Karniadakis, G., 2011, "Many-Body Dissipative Particle Dynamics Simulation of Liquid/Vapor and Liquid/Solid Interactions," J. Chem. Phys., **134**(20), p. 204114.

[19] Arienti, M., Wenzel, E. A., Sforzo, B. A., and Powell, C. F., 2021, "Effects of Detailed Geometry and Real Fluid Thermodynamics on Spray G Atomization," Proc. Combust. Inst., **38**(2), pp. 3277–3285.

[20] Abramzon, B., and Sirignano, W. A., 1989, "Droplet Vaporization Model for Spray Combustion Calculations," Int. J. Heat Mass Transfer, **32**(9), pp. 1605–1618.

[21] Tonini, S., 2006, "Fuel Spray Modeling in Direct-Injection Diesel and Gasoline Engines," Ph.D. thesis, City University London, London, UK.

[22] Hubbard, G. L., Denny, V. E., and Mills, A. F., 1975, "Droplet Evaporation: Effects of Transients and Variable Properties," Int. J. Heat Mass Transfer, **18**(9), pp. 1003–1008.

[23] Ge, W., Sankaran, R., and Chen, J. H., 2020, "Development of a CPU/GPU Portable Software Library for Lagrangian–Eulerian Simulations of Liquid Sprays," Int. J. Multiphase Flow, **128**, p. 103293.

[24] Liu, A. B., Mather, D., and Reitz, R. D., 1993, "Modeling the Effects of Drop Drag and Breakup on Fuel Sprays," SAE Paper No. 930072.

[25] Mueller, M. E., Blanquart, G., and Pitsch, H., 2009, "A Joint Volume-Surface Model of Soot Aggregation With the Method of Moments," Proc. Combust. Inst., **32**(1), pp. 785–792.

[26] Mueller, M. E., Blanquart, G., and Pitsch, H., 2011, "Modeling the Oxidation-Induced Fragmentation of Soot Aggregates in Laminar Flames," Proc. Combust. Inst., **33**(1), pp. 667–674.

[27] Modest, M. F., 2023, "Radiative Heat Transfer in Turbulent Combustion 2021 Max Jakob Memorial Award Paper," ASME J. Heat Mass Transfer-Trans. ASME, **145**(7), p. 073101.

[28] Charalampopoulos, T. T., Chang, H., and Stagg, B., 1989, "The Effects of Temperature and Composition on the Complex Refractive Index of Flame Soot," Fuel, **68**(9), pp. 1173–1179.

[29] Miniati, F., and Colella, P., 2007, "Block Structured Adaptive Mesh and Time Refinement for Hybrid, Hyperbolic+N-Body Systems," J. Comput. Phys., **227**(1), pp. 400–430.

[30] Quinn, T., Katz, N., Stadel, J., and Lake, G., 1997, "Time Stepping N-Body Simulations," arXiv:astro-ph/9710043

[31] Falgout, R. D., Jones, J. E., and Yang, U. M., 2006, "The Design and Implementation of Hypre, a Library of Parallel High Performance Pre-conditioners," Numerical Solution of Partial Differential Equations on Parallel Computers, Springer, Berlin, Heidelberg, pp. 267–294.

[32] Balay, S., Abhyankar, S., Adams, M. F., Benson, S., Brown, J., Brune, P., Buschelman, K., Constantinescu, E., Dalcin, L., and Dener, A., 2023, "PETSc/TAO Users Manual Revision 3.19," Argonne National Lab.(ANL), Argonne, IL.

[33] Briggs, W. L., Henson, V. E., and McCormick, S. F., 2000, A Multigrid Tutorial, 2nd ed., SIAM, Philadelphia, PA.

[34] Almgren, A. S., Bell, J. B., Colella, P., Howell, L. H., and Welcome, M. L., 1998, "A Conservative Adaptive Projection Method for the Variable Density Incompressible Navier–Stokes Equations," J. Computat. Phys., **142**(1), pp. 1–46.

[35] Daïf, A., Bouaziz, M., Chesneau, X., and Ali Chérif, A., 1998, "Comparison of Multicomponent Fuel Droplet Vaporization Experiments in Forced Convection With the Sirignano Model," Exp. Therm. Fluid Sci., **18**(4), pp. 282–290.

[36] Pickett, L. M., and Abraham, J. P., 2010, "Computed and Measured Fuel Vapor Distribution in a Diesel Spray," At. Sprays, **20**(3), pp. 241–250.

[37] National Institute of Standards and Technology, 2001, Security Requirements for Cryptographic Modules," Federal Information Processing Standards Publications (FIPS PUBS) 140-2, Change Notice 2 December 3, 2002, U.S. Department of Commerce, Washington, DC.

[38] Beale, J. C., and Reitz, R. D., 1999, "Modeling Spray Atomization With the Kelvin-Helmholtz/Rayleigh-Taylor Hybrid Model," At. Sprays, **9**(6), pp. 623–650.

[39] Nguyen, T. M., Dahms, R. N., Pickett, L. M., and Tagliante, F., 2022, "The Corrected Distortion Model for Lagrangian Spray Simulation of Transcritical Fuel Injection," Int. J. Multiphase Flow, **148**, p. 103927.

[40] Pickett, L. M., Manin, J., Genzale, C. L., Siebers, D. L., Musculus, M. P., and Idicheria, C. A., 2011, "Relationship Between Diesel Fuel Spray Vapor Penetration/Dispersion and Local Fuel Mixture Fraction," SAE Int. J. Engines, **4**(1), pp. 764–799.

[41] Roache, P. J., 2002, "Code Verification by the Method of Manufactured Solutions," ASME J. Fluids Eng., **124**(1), pp. 4–10.

[42] Goodwin, D. G., Speth, R. L., Moffat, H. K., and Weber, B. W., 2021, "Cantera: An Object-Oriented Software Toolkit for Chemical Kinetics, Thermodynamics, and Transport Processes," Version, 2.5.1.

[43] Pitsch, H., "FlameMaster, a C++ Computer Program for 0D Combustion and 1D Laminar Flame Calculations,".

[44] Bisetti, F., Blanquart, G., Mueller, M. E., and Pitsch, H., 2012, "On the Formation and Early Evolution of Soot in Turbulent Nonpremixed Flames," Combust. Flame, **159**(1), pp. 317–335.

[45] Blanquart, G., Pepiot-Desjardins, P., and Pitsch, H., 2009, "Chemical Mechanism for High Temperature Combustion of Engine Relevant Fuels With Emphasis on Soot Precursors," Combust. Flame, **156**(3), pp. 588–607.

[46] Xu, F., Sunderland, P., and Faeth, G., 1997, "Soot Formation in Laminar Premixed Ethylene/Air Flames at Atmospheric Pressure," Combust. Flame, **108**(4), pp. 471–493.

[47] Menon, A. V., Lee, S. Y., Linevsky, M. J., Litzinger, T. A., and Santoro, R. J., 2007, "Addition of NO2 to a Laminar Premixed Ethylene-Air Flame: Effect on Soot Formation," Proc. Combust. Inst., **31**(1), pp. 593–601.

[48] D'Anna, A., Rolando, A., Allouis, C., Minutolo, P., and D'Alessio, A., 2005, "Nano-Organic Carbon and Soot Particle Measurements in a Laminar Ethylene Diffusion Flame," Proc. Combust. Inst., **30**(1), pp. 1449–1456.

[49] D'Anna, A., and Kent, J. H., 2008, "A Model of Particular and Species Formation Applied to Laminar, Nonpremixed Flames for Three Aliphatic-Hydrocarbon Fuels," Combust. Flame, **152**(4), pp. 573–587.

[50] Zhang, J., Shaddix, C. R., and Schefer, R. W., 2011, "Design of "Model-Friendly" Turbulent Non-Premixed Jet Burners for C2+ Hydrocarbon Fuels," Rev. Sci. Instrum., **82**(7), p. 074101.

[51] Lignell, D. O., Chen, J. H., and Smith, P. J., 2008, "Three-Dimensional Direct Numerical Simulation of Soot Formation and Transport in a Temporally Evolving Nonpremixed Ethylene Jet Flame," Combust. Flame, **155**(1–2), pp. 316–333.

[52] Attili, A., Bisetti, F., Mueller, M. E., and Pitsch, H., 2014, "Formation, Growth, and Transport of Soot in a Three-Dimensional Turbulent Non-Premixed Jet Flame," Combust. Flame, **161**(7), pp. 1849–1865.

[53] Smooke, M., Long, M., Connelly, B., Colket, M., and Hall, R., 2005, "Soot Formation in Laminar Diffusion Flames," Combust. Flame, **143**(4), pp. 613–628.

[54] Colket, M., Heyne, J., Rumizen, M., Gupta, M., Edwards, T., Roquemore, W. M., Andac, G., Boehm, R., Lovett, J., Williams, R., Condevaux, J., Turner, D., Rizk, N., Tishkoff, J., Li, C., Moder, J., Friend, D., and Sankaran, V., 2017, "Overview of the National Jet Fuels Combustion Program," AIAA J., **55**(4), pp. 1087–1104.

[55] El Helou, I., Foale, J. M., Pathania, R. S., Ciardiello, R., Skiba, A. W., and Mastorakos, E., 2023, "A Comparison Between Fossil and Synthetic Kerosene Flames From the Perspective of Soot Emissions in a Swirl Spray RQL Burner," Fuel, **331**, p. 125608.

[56] Ryu, J. I., Kim, K., Min, K., Scarcelli, R., Som, S., Kim, K. S., Temme, J. E., Kweon, C.-B. M., and Lee, T., 2021, "Data-Driven Chemical Kinetic Reaction Mechanism for F-24 Jet Fuel Ignition," Fuel, **290**, p. 119508.

[57] Kim, K., Ryu, J. I., McGann, B., Min, K., Temme, J., Kweon, C.-B., and Lee, T., 2021, "Data-Driven Combustion Kinetic Modeling Concept of Alternative Alcohol-to-Jet (ATJ) Fuel," AIAA Paper No. 2021–1245.

[58] Edwards, J. T., 2017, "Reference Jet Fuels for Combustion Testing," AIAA Paper No. 2017–0146.

[59] Foale, J. M., 2022, Simulating Extinction and Blow-Off in Kerosene Swirl Spray Flames, Apollo–University of Cambridge Repository.

[60] Foale, J. M., Giusti, A., and Mastorakos, E., 2021, "Simulating the Blowoff Transient of a Swirling, Bluff Body-Stabilized Kerosene Spray Flame Using Detailed Chemistry," AIAA Paper No. 2021–0187.

[61] Bonanni, M., and Ihme, M., 2023, "Interaction of Preferential Evaporation and Low-Temperature Chemistry in Multicomponent Counterflow Spray Flames," Proc. Combust. Inst., **39**(2), pp. 2565–2573.

[62] Lee, D., Fahey, D., Skowron, A., Allen, M., Burkhardt, U., Chen, Q., Doherty, S., et al., 2021, "The Contribution of Global Aviation to Anthropogenic Climate Forcing for 2000 to 2018," Atmos. Environ., **244**, p. 117834.

[63] Voigt, C., Kleine, J., Sauer, D., Moore, R. H., Bräuer, T., Le Clercq, P., Kaufmann, S., et al., 2021, "Cleaner Burning Aviation Fuels Can Reduce Contrail Cloudiness," Commun. Earth Environ., **2**(1), p. 114.

[64] Kärcher, B., and Yu, F., 2009, "Role of Aircraft Soot Emissions in Contrail Formation," Geophys. Res. Lett., **36**(1), p. 01804.

[65] Govindaraju, P. B., and Ihme, M., 2016, "Group Contribution Method for Multicomponent Evaporation With Application to Transportation Fuels," Int. J. Heat Mass Trans, **102**, pp. 833–845.